

# Measurement of $\pi^0\Lambda$ , $\bar{K}^0n$ , and $\pi^0\Sigma^0$ production in $K^-p$ interactions for $p_{K^-}$ between 514 and 750 MeV/c

S. Prakhov<sup>1</sup>, B. M. K. Nefkens<sup>1</sup>, V. Bekrenev<sup>2</sup>, W. J. Briscoe<sup>3</sup>, N. Knecht<sup>4\*</sup>, A. Koulbardis<sup>2</sup>, N. Kozlenko<sup>2</sup>, S. Kruglov<sup>2</sup>, G. Lolos<sup>4</sup>, I. Lopatin<sup>2</sup>, A. Marušić<sup>1†</sup>, S. McDonald<sup>1‡</sup>, D. Peaslee<sup>5§</sup>, N. Phaisangittisakul<sup>1</sup>, J. W. Price<sup>1</sup>, A. Shafi<sup>3</sup>, A. Starostin<sup>1</sup>, H. M. Staudenmaier<sup>6</sup>, I. I. Strakovsky<sup>3</sup>, and I. Supek<sup>7</sup>

<sup>1</sup>University of California Los Angeles, Los Angeles, California 90095-1547, USA

<sup>2</sup>Petersburg Nuclear Physics Institute, Gatchina 188350, Russia

<sup>3</sup>The George Washington University, Washington, D.C. 20052-0001, USA

<sup>4</sup>University of Regina, Saskatchewan, Canada, S4S 0A2

<sup>5</sup>University of Maryland, College Park, Maryland 20742-4111, USA

<sup>6</sup>Universität Karlsruhe, Karlsruhe 76128, Germany and

<sup>7</sup>Rudjer Boskovic Institute, 10000 Zagreb, Croatia

(Dated: February 12, 2022)

Differential cross sections and hyperon polarizations have been measured for  $\bar{K}^0n$ ,  $\pi^0\Lambda$ , and  $\pi^0\Sigma^0$  production in  $K^-p$  interactions at eight  $K^-$  momenta between 514 and 750 MeV/c. The experiment detected the multiphoton final states with the Crystal Ball spectrometer using a  $K^-$  beam from the Alternating Gradient Synchrotron of BNL. The results provide significantly greater precision than the existing data, allowing a detailed reexamination of the excited hyperon states in our energy range.

PACS numbers: 25.80.Nv, 13.75.Jz, 13.30.Eg, 14.20.Jn

## I. INTRODUCTION

SU(3) Flavor Symmetry, FS, is a feature of QCD in the limit of vanishing quark masses. It implies many spectacular relations in baryon spectroscopy. For instance, it relates  $d\sigma(K^-p \rightarrow \eta\Lambda)$  to  $d\sigma(\pi^-p \rightarrow \eta n)$  and  $d\sigma(K^-p \rightarrow \pi^0\pi^0\Lambda)$  to  $d\sigma(\pi^-p \rightarrow \pi^0\pi^0n)$ . It also relates the width of flavor-symmetric states, such as  $\Sigma(1385)_{\frac{3}{2}}^+$  and  $\Delta(1232)_{\frac{3}{2}}^+$ . FS implies that, for every three-quark  $N^*$  resonance, there exists its flavor-symmetric  $\Lambda^*$  state, which should have the same spin and parity as the  $N^*$  and have the flavor structure of SU(3) octet members. The mass of the  $\Lambda^*$  resonance should be larger than that of the  $N^*$  by the constituent  $s-d$  quark-mass difference, which is about 140 MeV. Furthermore, there could exist also a  $\Lambda^*$  that is a SU(3) flavor singlet. However, the  $\Lambda^*$  singlet does not exist because it is not allowed as a consequence of color symmetry. FS also predicts that a triplet of  $\Sigma^*$  states should exist for every  $N^*$  octet and  $\Delta^*$  decuplet.

The Review of Particle Properties [1] lists several candidates for  $\Sigma^*$  states in the energy range between 1.5 and 1.7 GeV, the parameters of which are not well-established, and their status is still controversial. Three of these states, the one-star  $\Sigma(1480)$  and the two-star  $\Sigma(1560)$  with unknown  $J^P$  and the one-star  $\Sigma(1580)_{\frac{3}{2}}^-$ , cannot fulfill the requirements of FS and are therefore

candidates for being either exotic states, such as five-quark states, or a hybrid state with an important gluon component in the wave function. This situation is a consequence of the lack of reliable data on  $K^-p$  interactions [2, 3, 4, 5], especially for the reactions that have several neutral particles in the final state.

The experimental study of the reactions  $K^-p \rightarrow$  *neutrals* was performed with the Crystal Ball (CB) multiphoton spectrometer at the Alternating Gradient Synchrotron (AGS), aiming at a substantial improvement of the hyperon-spectroscopy field. The major interest was in the production of the  $\eta\Lambda$ ,  $\bar{K}^0n$ ,  $\pi^0\Lambda$ ,  $\pi^0\Sigma^0$ ,  $\pi^0\pi^0\Lambda$ , and  $\pi^0\pi^0\Sigma^0$  final states. In these reactions, the experimental situation was especially poor for the  $\pi^0\Sigma^0(\rightarrow \pi^0\gamma\Lambda)$ ,  $\pi^0\pi^0\Lambda$ , and  $\pi^0\pi^0\Sigma^0$  production. These final states have more than one neutral particle and could not be measured in the old bubble-chamber experiments. Our results on the  $\eta\Lambda$ ,  $\pi^0\pi^0\Lambda$ , and  $\pi^0\pi^0\Sigma^0$  production in  $K^-p$  interactions at eight incident  $K^-$  momenta between 514 and 750 MeV/c have been reported in Refs. [6, 7, 8]. An analysis of our  $K^-p \rightarrow \pi^0\Lambda$  data in the c.m. energy range 1565 to 1600 MeV to test the existence of the  $\Sigma(1580)_{\frac{3}{2}}^-$  state has been presented in Ref. [9]. An independent analysis of the  $K^-p \rightarrow \pi^0\Sigma^0$  reaction, using the same data set, was recently presented in Ref. [10]. Another independent analysis of the  $K^-p \rightarrow \bar{K}^0n$  and  $K^-p \rightarrow \pi^0\Lambda$  reactions was presented in Ref. [11]. In the present work, we report the experimental results on  $\bar{K}^0n$ ,  $\pi^0\Lambda$ , and  $\pi^0\Sigma^0$  production in  $K^-p$  interactions at eight incident  $K^-$  momenta between 514 and 750 MeV/c. Compared to the analyses of Refs. [10, 11], our analysis uses kinematic fitting as a part of the event reconstruction. The subtraction of background reactions is based on our own measurement of them. In contrast to Ref. [10], we use the full fiducial volume of the CB spectrometer, which provides us with much larger statistics and non-zero acceptance for the forward production angles. A

\*Present address: Physics Dept. of University of Toronto, 60 St. George St., Toronto, Ontario, Canada, M5S 1A7

†Present address: Collider-Accelerator Dept., Brookhaven National Laboratory, Upton, NY 11973, USA.

‡Present address: TRIUMF, 4004 Wesbrook Mall, Vancouver, B.C., Canada, V6T 2A3.

§Deceased

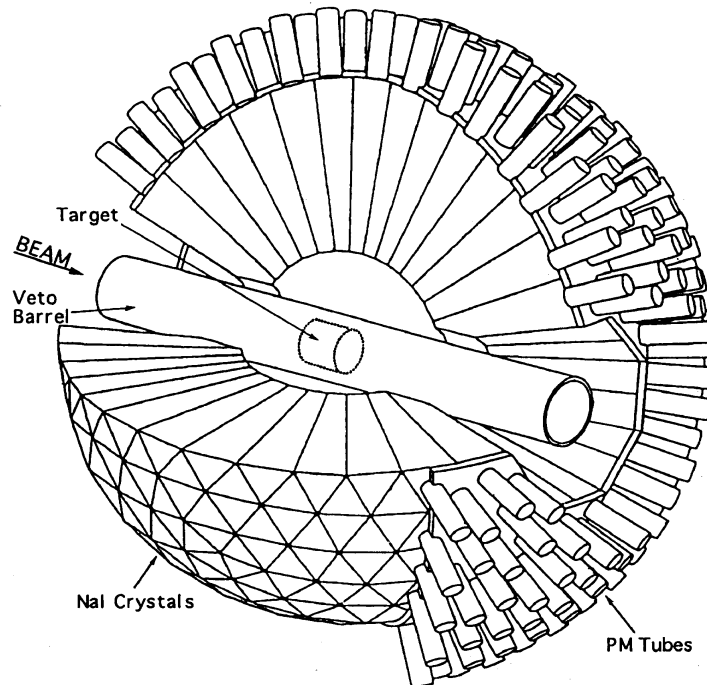


FIG. 1: Layout of the Crystal Ball spectrometer.

new Partial Wave Analysis (PWA), involving our results on the differential cross sections for  $\bar{K}^0 n$ ,  $\pi^0 \Lambda$ , and  $\pi^0 \Sigma^0$  production in  $K^- p$  interactions and the polarizations of  $\Lambda$  and  $\Sigma^0$ , is planned. This PWA is expected to improve the parameters of the low-mass  $\Lambda^*$  and  $\Sigma^*$  states.

## II. EXPERIMENTAL ARRANGEMENTS

The Crystal Ball multiphoton spectrometer was installed in the C6 beam line of the AGS at Brookhaven National Laboratory. The CB spectrometer is a highly-segmented sphere of 672 NaI(Tl) crystals (see Fig. 1). The sphere has an entrance and exit tunnel for the beam and a 50-cm-diameter spherical cavity in the center. The solid angle covered by the CB is 93% of  $4\pi$  steradian. The CB crystals are packed in two hermetically sealed and evacuated hemispheres. The crystals have the shape of truncated triangular pyramid (see Fig. 2), all pointed towards the center of the CB.

The crystal length is 40.6 cm, which corresponds to 15.7 radiation lengths. The pulse height in every crystal was measured with individual ADCs (analog-to-digital converter). For registering the timing information, one TDC (time-to-digital converter) was used for every minor triangle, which is a group of nine neighboring crystals. The typical energy resolution for electromagnetic showers in the CB was  $\Delta E/E = 0.020/(E[\text{GeV}])^{0.36}$ . The directions of the photon showers were measured with a resolution in  $\theta$  (the polar angle with respect to the beam axis) of  $\sigma_\theta = 2^\circ - 3^\circ$ , under the assumption that the photons are produced in the center of the CB. The resolution in azimuthal angle  $\phi$  is  $\sigma_\phi/\sin\theta$ . The angular resolutions are mainly defined by the granularity of the CB and do not depend

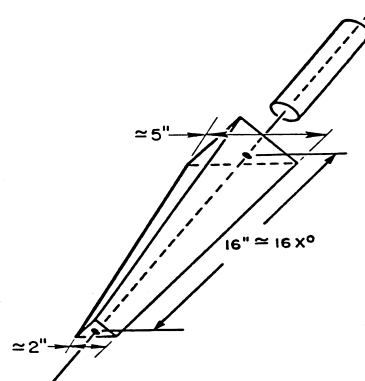


FIG. 2: Dimensions of the CB crystal.

on the energy resolution of the CB crystals. The situation is slightly different when a photon is produced not in the center of the CB. In this case, the real angles of the photon must be calculated from an interaction point (which can be either the primary vertex of the event in the target or the secondary vertex of the outgoing particles decaying in flight) to the point inside the CB that is determined by the depth of the electromagnetic shower in the NaI(Tl) material. Also, the energy and angular resolution of the CB becomes somewhat worse when a photon hits the crystals close to the CB beam tunnels. In this case, part of the electromagnetic shower can leak through the side surface of the so-called “guard” crystals (i.e., the crystals that form the inner surface of the tunnels).

The C6 line provided a beam of negative kaons and pions with the  $K^-/\pi^-$  ratio enhanced to about 0.1 by two

electrostatic separators. Beam particles were incident on a 10-cm-long liquid-hydrogen (LH<sub>2</sub>) target located in the center of the Crystal Ball. The beam divergences on the target were  $\sigma_X \approx 2.5$  cm and  $\sigma_Y \approx 2$  cm. The diameter of the target was 10 cm. The determination of the beam momentum was done with a dipole magnet and a set of four multiwire drift chambers. One of the chambers was located upstream and the other three downstream of the magnet. The coordinate resolution of the chambers was  $\sigma_X \approx \sigma_Y \approx 0.2$  mm. The momentum resolution  $\sigma_p/p$  for an individual incident kaon varied from 0.6% to 1.%, depending on the momentum value. The largest contribution to the uncertainty in the incident-particle momentum comes from the kaon multiple scattering and energy losses in the beam counters and the LH<sub>2</sub> target. The mean value  $p_{K^-}$  for the incident-momentum spectra and the momentum spread  $\sigma_p$ , which were determined at the target center, are listed in Table I. The uncertainty in determining the mean beam momentum is 2–3 MeV/c. This uncertainty is mainly caused by the precision of the calculation of the magnetic field in the dipole magnet and the energy loss of the incident kaons before they interact in the target.

To monitor the beam particles, a system of plastic scintillation counters was used. This system included the  $S_1$  hodoscope upstream and the  $S_2$  counter downstream of the dipole magnet, and the  $S_T$  counter located 162 cm upstream of the LH<sub>2</sub> target. The coincidence of signals from  $S_1$ ,  $S_2$  and  $S_T$  served as the beam trigger. The time-of-flight of beam particles between  $S_1$  and  $S_T$  was used in the trigger and also in the off-line analysis to suppress the background from pion interactions in the target.

The LH<sub>2</sub> target was surrounded by a 16-cm-diameter “barrel” made of four plastic scintillation counters that functioned as a veto for the beam interactions with charged particles in the final state. The 120-cm length of the veto-barrel counters ensured almost 100% rejection of those events. The 5-mm thickness of the counters implied both a good efficiency of the veto barrel for the charged-particle detection and a low probability for photon conversion.

The CB event trigger was the beam trigger in coincidence with a CB energy trigger, which required the total energy deposited in the crystals to exceed a certain threshold. The first two layers of the crystals in the CB tunnels (i.e., closest to the beam line), which had a high occupancy from beam-halo interactions, were excluded from the CB energy trigger. The CB neutral-event trigger required the anti-coincidence of the CB event trigger with signals from the veto-barrel counters.

More details about the CB setup at the AGS and its  $K^-p$ -data analyses can be found in Refs. [6, 7, 8, 9, 10, 11, 12, 13].

### III. DATA ANALYSIS

Since the Crystal Ball detector is designed as a multi-photon spectrometer,  $K^-p$  interactions were studied by measuring the photons and the neutron in the final state. The  $\bar{K}^0$  meson and the  $\Lambda$  and  $\Sigma^0$  hyperons were measured in the CB by the decay chains  $K_S^0 \rightarrow \pi^0\pi^0 \rightarrow 4\gamma$ ,

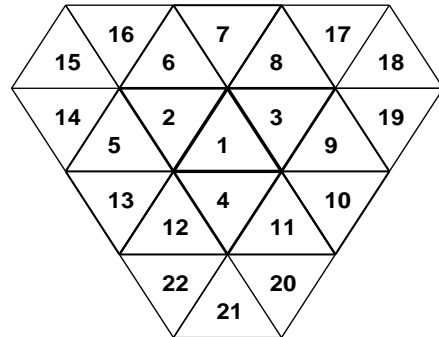


FIG. 3: Configuration of a cluster in the CB.

$\Lambda \rightarrow \pi^0 n \rightarrow 2\gamma n$ , and  $\Sigma^0 \rightarrow \gamma\Lambda \rightarrow \gamma\pi^0 n \rightarrow 3\gamma n$ . As the final-state photons produce electromagnetic showers in the NaI(Tl) crystals, they can be recognized as so-called “clusters” in the density of the energy deposited in the CB. The outgoing neutrons can also be detected if the products of their interactions in the NaI(Tl) material produce the ionization that is enough to form a cluster. In general, a cluster in the CB is defined as a group of neighboring crystals in which energy is deposited from the interaction of a photon, a charged particle, or a neutron produced in the final state. Clusters produced by different particle types have different features. Since our analysis involves mainly multi-photon final states, the cluster algorithm was optimized to reconstruct parameters of a photon from its electromagnetic shower with good energy and angular resolution and with a reasonable separation between shower split-offs and overlapping showers. The software threshold for the cluster energy was chosen to be 20 MeV; this value optimizes the yield of the reconstructed events for the  $K^-p \rightarrow \text{neutrals}$  processes under study. The size of one cluster was limited to a configuration of 22 crystals (see Fig. 3), which is large enough to contain the full spread of a photon shower at our energies. Cluster directions were measured as the weighted average of the directions of all crystals forming the cluster. The weight factor of each crystal in this average was taken as the square root of the crystal energy,  $\sqrt{E}$ .

As the decay time of NaI(Tl) is about 250 ns, the high intensity of the incident beam causes good events to be contaminated by so-called pile-up clusters (i.e., the clusters remaining from other events). Since the pile-up clusters change the proper number of the clusters expected in the CB from good events, such events can be lost from consideration unless the pile-up clusters are eliminated. Elimination of the pile-up clusters was based on the TDC information of the crystals forming the clusters. Since our good events cause the CB trigger, their clusters have times that are peaked in a restricted timing window. All clusters that occur outside this window were eliminated from further consideration. The loss of good events due to the pile-up clusters inside the window were estimated by varying the window width.

The kinematic-fitting technique was used to select candidates for the reactions that were studied. In the present

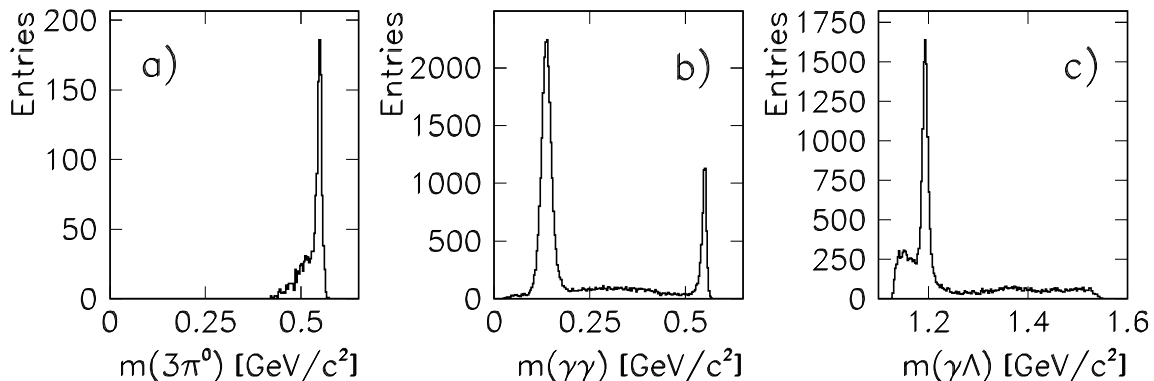


FIG. 4: The invariant-mass spectra for the experimental events at  $p_{K^-} = 750$  MeV/c selected by testing the following hypotheses with the kinematic fit: (a)  $K^-p \rightarrow \pi^0\pi^0\pi^0\Lambda \rightarrow 4\pi^0n \rightarrow 8\gamma n$ , where  $\sigma_m(\eta \rightarrow 3\pi^0) \approx 5$  MeV/c<sup>2</sup>; (b)  $K^-p \rightarrow \gamma\gamma\Lambda \rightarrow \gamma\gamma\pi^0n \rightarrow 4\gamma n$ , where  $\sigma_m(\eta \rightarrow 2\gamma) \approx 6$  MeV/c<sup>2</sup> and  $\sigma_m(\pi^0 \rightarrow 2\gamma) \approx 13$  MeV/c<sup>2</sup>; and (c)  $K^-p \rightarrow \gamma\pi^0\Lambda \rightarrow \gamma\pi^0\pi^0n \rightarrow 5\gamma n$ , where  $\sigma_m(\Sigma^0 \rightarrow \gamma\Lambda) \approx 6$  MeV/c<sup>2</sup>.

analysis, every event with the proper cluster multiplicity was fitted to the following three hypotheses:

$$K^-p \rightarrow K_S^0n \rightarrow (\pi^0\pi^0)n \rightarrow 4\gamma n, \quad (1)$$

$$K^-p \rightarrow \pi^0\Lambda \rightarrow \pi^0(\pi^0n) \rightarrow 4\gamma n, \quad (2)$$

$$K^-p \rightarrow \pi^0\Sigma^0 \rightarrow \pi^0\gamma\Lambda \rightarrow \pi^0\pi^0\gamma n \rightarrow 5\gamma n. \quad (3)$$

The incident kaon was parameterized in the kinematic fit by five measured variables: momentum, angles  $\theta_x$  and  $\theta_y$ , and position coordinates  $x$  and  $y$  at the target. A photon cluster was parameterized by three measured variables: energy and angles  $\theta$  and  $\phi$ . As the data were taken with a 10-cm-long LH<sub>2</sub> target, the  $z$  coordinate of the vertex was a free variable of the kinematic fit. Including  $z$  into the fit improves the angular resolution of the photons. The cluster angles  $\theta$  and  $\phi$ , which were used in the minimization procedure, were calculated with respect to the CB center. The photon angles, used in the calculation of the kinematic constraints, were defined by the directions from the vertex coordinates to the point determined by the cluster angles and the effective depth of the photon shower in the NaI material. In our analysis, the effective depth of the electromagnetic shower was defined as the depth where a photon has likely deposited half its initial energy. For the neutron cluster, the effective depth was taken to be half the length of the crystals.

When the final-state neutron was not detected, its energy and two angles were free variables of the kinematic fit. For the neutron detected in the CB, the angles of its cluster were used as the measured variables and the neutron energy as a free variable. In our analysis of reactions (1), (2), and (3), the detection efficiency for the final-state neutron increases from 21% for our lowest beam momenta to 28% for the highest. Since the major ionization from the neutron passage in the crystals occurs due to recoil protons, the energy of the neutron cluster is very uncertain and cannot be used to reconstruct the

kinetic energy of the neutron. Many neutrons, especially low-energy ones, produce a signal in the CB that is below the 20-MeV-energy threshold used in the cluster reconstruction. The angular resolution of the CB for neutron clusters is slightly worse than for photon clusters.

Since all reactions in our analysis have a particle decaying in flight, the decay length of this particle was also a free variable of the kinematic fit. The corresponding secondary vertex was then determined from the primary-vertex coordinates, the direction of the decaying particle, and the decay length. The calculation of the angles of the final-state photons and neutron from the cluster angles, if they were produced from the secondary vertex, is the same as for the primary vertex.

The invariant-mass resolution of the CB after applying the kinematic-fitting technique is illustrated in Fig. 4. Three invariant-mass spectra are shown for our data at the beam momentum of 750 MeV/c after testing events for the following hypotheses:  $K^-p \rightarrow \pi^0\pi^0\pi^0\Lambda$ ,  $K^-p \rightarrow \gamma\gamma\Lambda$ , and  $K^-p \rightarrow \pi^0\gamma\Lambda$ , where the  $\Lambda$  hyperon was identified by its decay into  $\pi^0n$ . The invariant-mass resolution for the  $m(3\pi^0)$  peak from  $\eta$  decays has  $\sigma_m(3\pi^0) \approx 5$  MeV/c<sup>2</sup>, which is comparable to  $\sigma_m(\gamma\gamma) \approx 6$  MeV/c<sup>2</sup> from  $\eta \rightarrow \gamma\gamma$  decays. The  $m(\gamma\gamma)$  resolution for  $\pi^0 \rightarrow \gamma\gamma$  decays is about 13 MeV/c<sup>2</sup>. We cannot illustrate the  $m(\pi^0n)$  resolution for  $\Lambda \rightarrow \pi^0n$  decays as a constraint on the  $\Lambda$ -hyperon mass is used in the kinematic fit for the secondary-vertex determination. Instead, we show the  $m(\gamma\Lambda)$  peak from  $\Sigma^0$  decays, for which  $\sigma_m(\gamma\Lambda) \approx 6$  MeV/c<sup>2</sup>.

The candidates for reactions (1) and (2) were searched for in four-cluster and five-cluster events since these processes have the same final state, including four photons and the neutron. The four-cluster events were tested for the case when only the four photons were detected in the CB. The five-cluster events were tested for the case when all five final-state particles were detected. Similarly, the candidates for reaction (3), which have five photons and the neutron in the final state, were searched for in five-cluster and six-cluster events. The test of each hypoth-

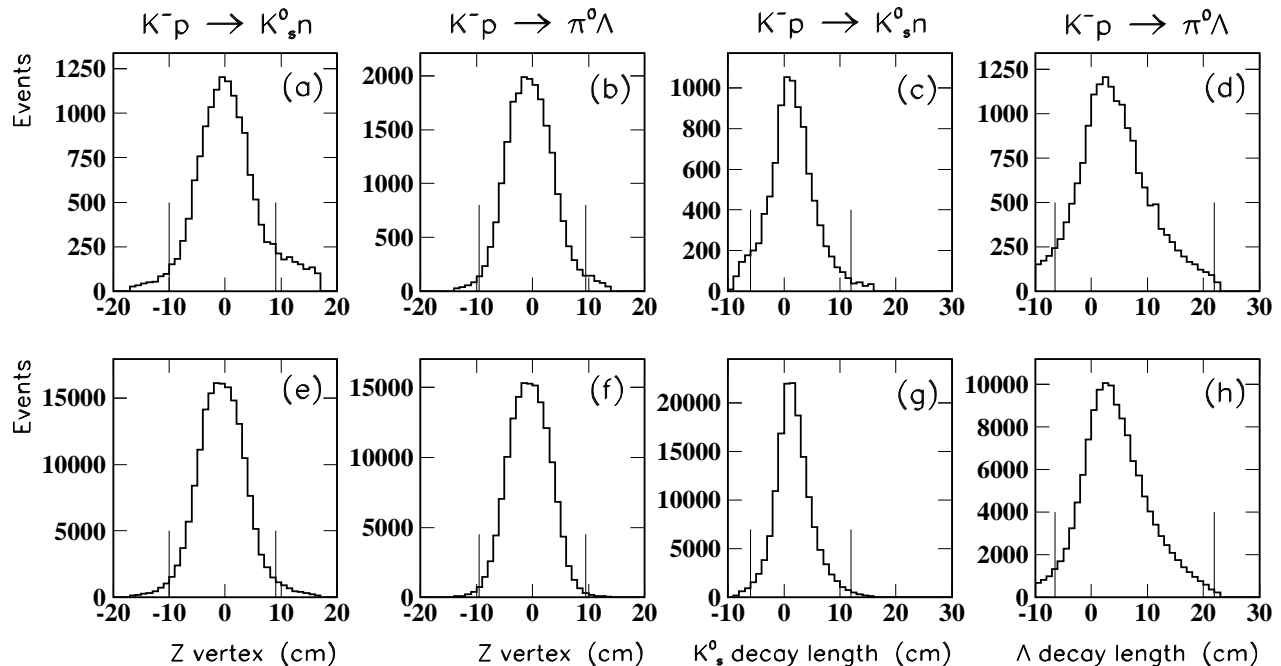


FIG. 5: Experimental (a-d) and MC (e-h) distributions for the  $z$  coordinate of the primary vertex in reaction (a,e)  $K^-p \rightarrow K_S^0 n$  and (b,f)  $K^-p \rightarrow \pi^0 \Lambda$ , and for the decay length of (c,g)  $K_S^0$  in reaction  $K^-p \rightarrow K_S^0 n$  and (d,h)  $\Lambda$  in reaction  $K^-p \rightarrow \pi^0 \Lambda$ . The events between the vertical lines shown in the figures are accepted for further analysis.

esis involves all possible permutations of assigning the detected clusters to the particles in the reaction chain. The events for which at least one permutation satisfied the tested hypothesis at the 2% confidence level, C.L., (i.e., with a probability larger than 2%) were accepted as the reaction candidates. The permutation with the largest C.L. was used to reconstruct the kinematics of the reaction.

The candidates selected for our three reactions are contaminated with backgrounds that must be subtracted in the analysis. The first source of background is from misidentification of events from different  $K^-p$  reactions. The second source is from processes that are not kaon interactions in the LH<sub>2</sub> target. The major fraction of these interactions are  $K^-$  decays in the beam. This background was investigated using data samples when the target was empty. The absolute contribution of this background was determined from the ratio of totals of the beam kaons incident on the full and empty target. The fraction of the so-called “empty-target” background, which left in the reaction candidates after all selection cuts, varies slightly depending on the beam momentum, the reaction itself, and the cuts applied. For our typical selection cuts, which are discussed later on in the text, the remaining empty-target background comprises 6% to 9% for the  $K_S^0 n$  and  $\pi^0 \Lambda$  candidates and 4% to 6% for the  $\pi^0 \Sigma^0$  candidates. This background was subtracted from our experimental production-angle distributions.

A Monte Carlo (MC) simulation of reactions (1), (2), and (3) was used to determine the experimental acceptance and to estimate the fraction of the background coming from misidentification of events from different

reactions. First, all reactions were simulated with an isotropic production-angle distribution. To reproduce the beam structure correctly, the information from the experimental beam-trigger events was used as the input for simulating the incident kaons. The MC events for each beam momentum were then propagated through a full GEANT (version 3.21) simulation of the CB detector, folded with the CB resolutions and trigger conditions, and analyzed the same way as the experimental data. The small difference between the experimental data and the MC simulation for the neutron response in the CB was not important, as we summed the events with and without the neutron detected.

The analysis of the MC simulation showed that the largest misidentification of events from different reactions is between processes (1) and (2), which have the same final state of four photons. However, for the events that satisfied both the hypotheses, the C.L. for the “true” one was typically larger than for the “false”. Therefore, to decrease the background of these reactions from each other to the level of 4% or less, we accepted only the hypothesis with the largest C.L., also requiring it to be at least twice as large as the C.L. for the second hypothesis. For further suppression of other backgrounds, tightening the cut on the C.L. of the reaction hypothesis itself can be applied. If the events of each the reaction are selected at the 5% C.L., the background from process (3) was found to be less than 1% for  $K_S^0 n$  events and less than 2% for  $\pi^0 \Lambda$  events. The  $\pi^0 \Sigma^0$  events were contaminated by a background from process (2) to the level less than 2%, and from processes (1) and  $K^-p \rightarrow \pi^0 \pi^0 \Lambda \rightarrow 3\pi^0 n$  to the level less than 1%.

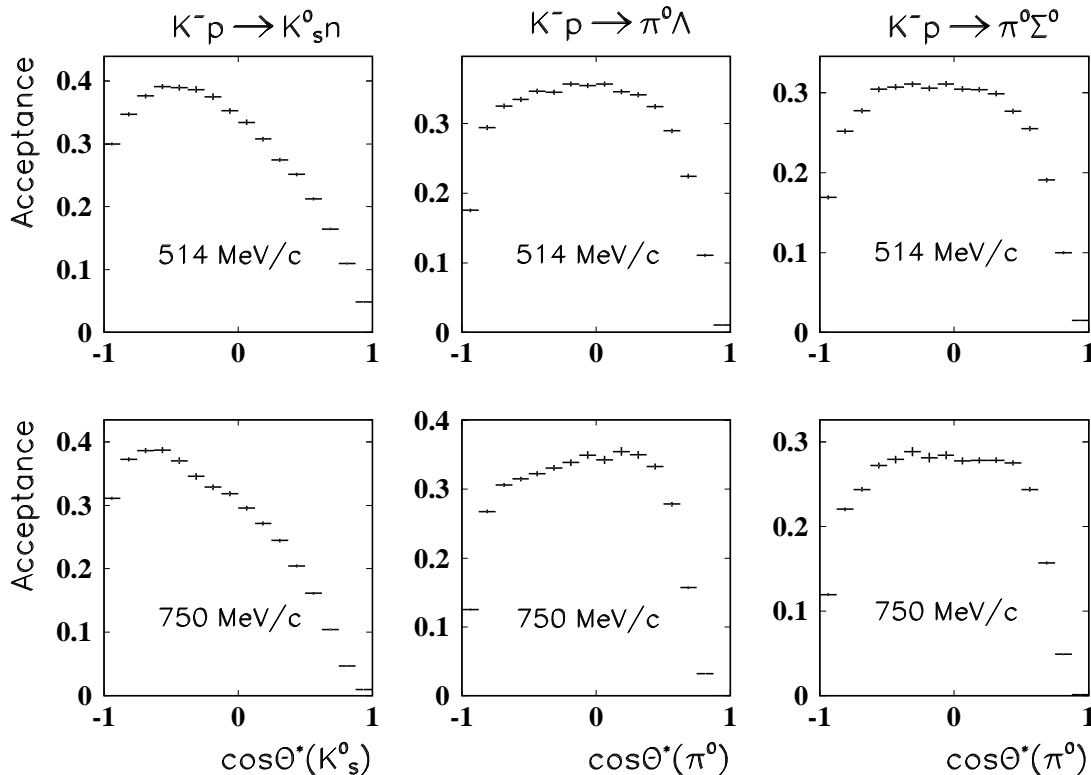


FIG. 6: The acceptance for the production angle  $\theta^*$  of the outgoing meson in the c.m. system; it is shown for reactions  $K^-p \rightarrow K_S^0 n$ ,  $K^-p \rightarrow \pi^0 \Lambda$ , and  $K^-p \rightarrow \pi^0 \Sigma^0$  at beam momenta of 514 and 750 MeV/c.

The low levels of the background contamination were achieved in part by applying a cut on the  $z$  coordinate of the primary vertex of the event and on the decay length of the  $K_S^0$  meson and the  $\Lambda$  hyperon. The  $z$ -coordinate and decay-length distributions together with the cuts are illustrated for the experimental data and the MC simulation in Fig. 5. The small difference between the experimental data and MC simulation is due to the remaining background that is not subtracted from the experimental distributions. The deviation of the  $z$  distributions from the target shape is determined by the resolution of the kinematic fit in  $z$ , which is about 2 cm. Similarly, the actual decay-length distributions are smeared with the resolution of 3 cm.

The acceptance for reactions  $K^-p \rightarrow K_S^0 n$ ,  $K^-p \rightarrow \pi^0 \Lambda$ , and  $K^-p \rightarrow \pi^0 \Sigma^0$  was determined as a function of  $\cos(\theta^*)$ , where  $\theta^*$  is the production angle of the final-state meson (i.e., the angle between the direction of the outgoing meson and the incident  $K^-$  meson) in the center-of-mass (c.m.) system. The acceptance for each of the studied reactions is shown in Fig. 6 for two beam momenta: 514 and 750 MeV/c. These acceptances include the effects of all our standard cuts used for the event selection. A poorer  $\cos(\theta^*)$  acceptance of the forward  $\theta^*$  angles for a higher beam momentum is mostly due to the larger threshold on the CB total energy in the event trigger. This threshold was 0.9 GeV for  $p_{K^-} = 514$  MeV/c and reached 1.5 GeV for  $p_{K^-} = 750$  MeV/c. The experimental resolution in  $\theta^*$  for  $K^-p \rightarrow K_S^0 n$  varies between  $6.5^\circ$  at  $p_{K^-} = 514$  MeV/c and  $4.5^\circ$  at  $p_{K^-} = 750$  MeV/c.

The  $\theta^*$  resolution for  $K^-p \rightarrow \pi^0 \Lambda$  and  $K^-p \rightarrow \pi^0 \Sigma^0$  varies between  $3.5^\circ$  at  $p_{K^-} = 514$  MeV/c and  $3.0^\circ$  at  $p_{K^-} = 750$  MeV/c.

The experimental  $\cos(\theta^*)$  distributions, which were obtained after the “empty-target” subtraction and the acceptance correction, were used to simulate reactions  $K^-p \rightarrow K_S^0 n$ ,  $K^-p \rightarrow \pi^0 \Lambda$ , and  $K^-p \rightarrow \pi^0 \Sigma^0$  with the realistic production-angle distributions. Then this MC simulation was used for the subtraction of the background remaining from the reaction misidentification.

The subtraction of the  $\pi^0 \pi^0 \Lambda$  background from the  $\pi^0 \Sigma^0$  spectra was based on the results of our analysis for  $K^-p \rightarrow \pi^0 \pi^0 \Lambda$  published in Ref. [7].

#### IV. EXPERIMENTAL RESULTS

The numbers of experimental events remaining after the subtraction of all backgrounds are listed for our three reactions and the eight beam momenta in Table I. The differential cross sections are given as a function of  $\cos(\theta^*)$ , where the full range from -1 to 1 is divided in 16 bins. The bins with the acceptance below 0.5% are not presented. To calculate our cross sections, the PDG [1] branching ratios  $0.358 \pm 0.005$  for the  $\Lambda \rightarrow \pi^0 n$  decay and  $0.3069 \pm 0.0005$  for the  $K_S^0 \rightarrow \pi^0 \pi^0$  decay were used. The effective proton density in the target times the effective target length was  $(4.05 \pm 0.08) \times 10^{-4}$  mb $^{-1}$ . The calculation of the total number of beam kaons incident on the target is given in detail in Ref. [14]. The uncertainties

TABLE I: Number of experimental events obtained for reactions  $K^-p \rightarrow K_S^0 n$ ,  $K^-p \rightarrow \pi^0 \Lambda$ , and  $K^-p \rightarrow \pi^0 \Sigma^0$  at the eight beam momenta.

$p_{K^-} \pm \sigma_p$ [MeV/c]	514±10	560±11	581±12	629±11	659±12	687±11	714±11	750±13
$N_{\text{Exp}}(K^-p \rightarrow K_S^0 n)$	2,514	5,007	6,968	7,711	7,903	8,245	8,157	10,134
$N_{\text{Exp}}(K^-p \rightarrow \pi^0 \Lambda)$	3,402	6,689	10,118	11,735	13,238	15,157	16,510	25,948
$N_{\text{Exp}}(K^-p \rightarrow \pi^0 \Sigma^0)$	2,702	5,041	7,269	7,484	8,092	8,964	9,684	14,010

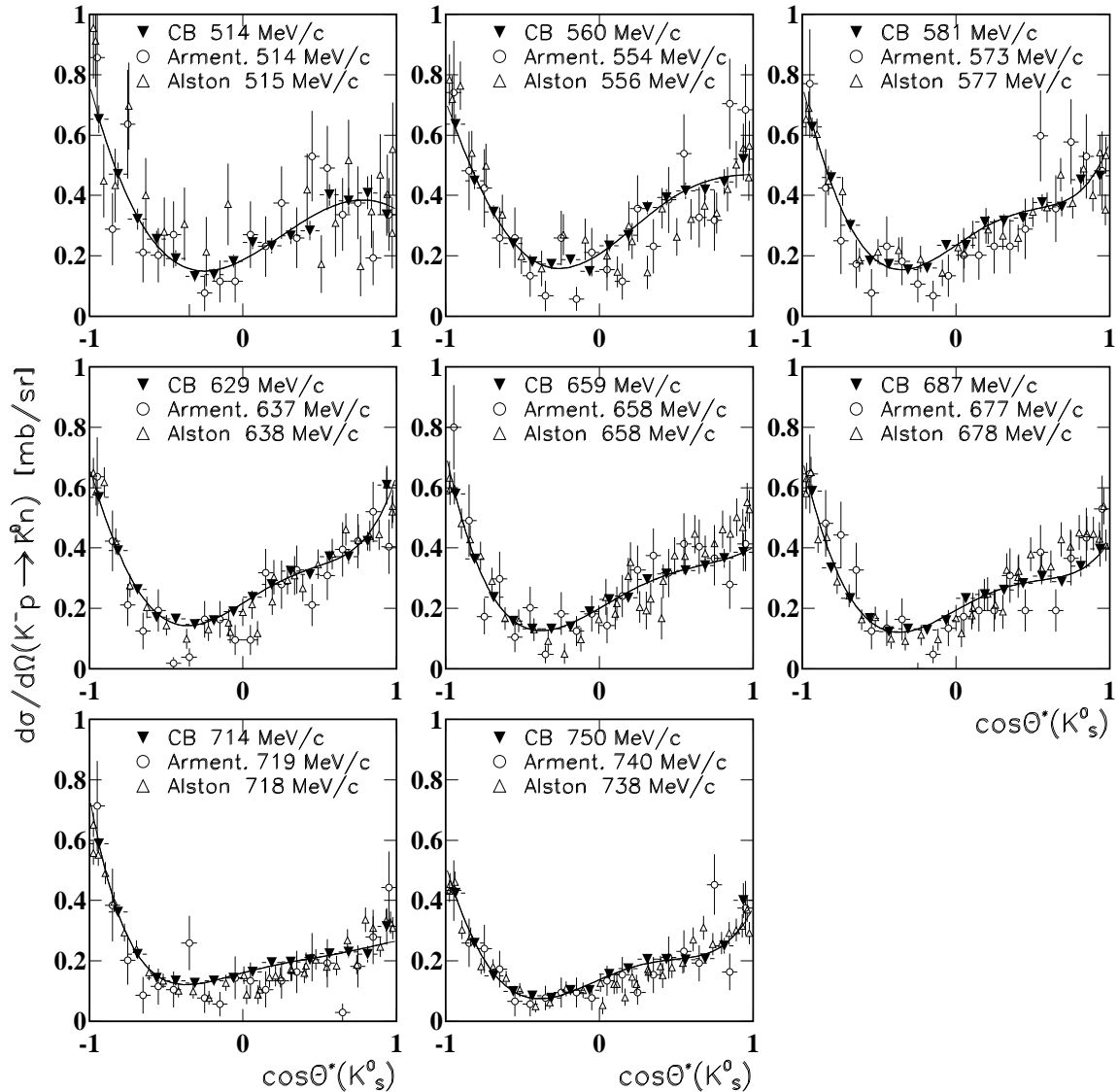


FIG. 7: Our differential cross sections for  $K^-p \rightarrow \bar{K}^0 n$  compared to the results of Armenteros [2] and Alston-Garnjost [4] for similar beam momenta. The curves are the Legendre polynomial fits of our data.

in our results for the differential cross sections are statistical only. The overall systematic uncertainty in the differential cross sections was estimated to be about 7%; it is not included in the errors presented. The major contributions to the systematic uncertainty come from the evaluation of the losses of good events due to pile-up clusters and from the uncertainty in the total number of

beam kaons incident on the target.

Our differential cross sections for  $K^-p \rightarrow \bar{K}^0 n$  as a function of  $\cos(\theta^*)$  for  $\bar{K}^0$  are given for each of the eight beam momenta in Tables II and III. Our differential cross sections for  $K^-p \rightarrow \bar{K}^0 n$  are compared in Fig. 7 to the results of Armenteros [2] and Alston-Garnjost [4] for similar beam momenta. The results of Armenteros [2]

TABLE II: Differential cross sections for the  $K^-p \rightarrow \bar{K}^0n$  reaction for the four lowest beam momenta.

$p_{K^-} \pm \delta_p$ [MeV/c]	514 ± 10	560 ± 11	581 ± 12	629 ± 11
$\cos \theta^*(\bar{K}^0)$	$d\sigma/d\Omega$ [mb/sr]	$d\sigma/d\Omega$ [mb/sr]	$d\sigma/d\Omega$ [mb/sr]	$d\sigma/d\Omega$ [mb/sr]
-0.94	0.653 ± 0.046	0.636 ± 0.033	0.626 ± 0.032	0.568 ± 0.022
-0.81	0.471 ± 0.039	0.449 ± 0.028	0.459 ± 0.025	0.391 ± 0.017
-0.69	0.322 ± 0.035	0.346 ± 0.022	0.301 ± 0.022	0.263 ± 0.014
-0.56	0.255 ± 0.028	0.241 ± 0.018	0.183 ± 0.018	0.171 ± 0.011
-0.44	0.192 ± 0.027	0.181 ± 0.016	0.173 ± 0.013	0.165 ± 0.010
-0.31	0.133 ± 0.019	0.172 ± 0.015	0.155 ± 0.013	0.147 ± 0.009
-0.19	0.138 ± 0.020	0.188 ± 0.015	0.159 ± 0.017	0.160 ± 0.010
-0.06	0.182 ± 0.021	0.149 ± 0.015	0.235 ± 0.015	0.190 ± 0.011
0.06	0.245 ± 0.023	0.234 ± 0.018	0.236 ± 0.018	0.237 ± 0.013
0.19	0.233 ± 0.026	0.269 ± 0.019	0.313 ± 0.019	0.279 ± 0.014
0.31	0.267 ± 0.027	0.360 ± 0.023	0.317 ± 0.022	0.323 ± 0.016
0.44	0.284 ± 0.033	0.394 ± 0.027	0.325 ± 0.026	0.313 ± 0.017
0.56	0.402 ± 0.037	0.415 ± 0.028	0.377 ± 0.027	0.371 ± 0.020
0.69	0.382 ± 0.042	0.418 ± 0.034	0.363 ± 0.032	0.372 ± 0.025
0.81	0.408 ± 0.054	0.444 ± 0.043	0.453 ± 0.041	0.424 ± 0.032
0.94	0.337 ± 0.069	0.521 ± 0.071	0.466 ± 0.063	0.609 ± 0.064

TABLE III: Differential cross sections for the  $K^-p \rightarrow \bar{K}^0n$  reaction for the four highest beam momenta.

$p_{K^-} \pm \delta_p$ [MeV/c]	659 ± 12	687 ± 11	714 ± 11	750 ± 13
$\cos \theta^*(\bar{K}^0)$	$d\sigma/d\Omega$ [mb/sr]	$d\sigma/d\Omega$ [mb/sr]	$d\sigma/d\Omega$ [mb/sr]	$d\sigma/d\Omega$ [mb/sr]
-0.94	0.578 ± 0.020	0.588 ± 0.022	0.589 ± 0.019	0.425 ± 0.014
-0.81	0.363 ± 0.017	0.335 ± 0.019	0.362 ± 0.014	0.260 ± 0.010
-0.69	0.237 ± 0.013	0.233 ± 0.015	0.222 ± 0.011	0.150 ± 0.008
-0.56	0.159 ± 0.010	0.167 ± 0.010	0.144 ± 0.008	0.100 ± 0.006
-0.44	0.132 ± 0.010	0.123 ± 0.011	0.134 ± 0.008	0.085 ± 0.006
-0.31	0.132 ± 0.010	0.132 ± 0.009	0.127 ± 0.009	0.077 ± 0.006
-0.19	0.140 ± 0.010	0.129 ± 0.011	0.135 ± 0.008	0.104 ± 0.007
-0.06	0.190 ± 0.011	0.159 ± 0.011	0.144 ± 0.009	0.103 ± 0.007
0.06	0.229 ± 0.013	0.233 ± 0.012	0.165 ± 0.010	0.156 ± 0.008
0.19	0.236 ± 0.014	0.246 ± 0.012	0.195 ± 0.011	0.175 ± 0.008
0.31	0.296 ± 0.015	0.261 ± 0.015	0.196 ± 0.012	0.207 ± 0.010
0.44	0.315 ± 0.017	0.283 ± 0.016	0.204 ± 0.013	0.206 ± 0.011
0.56	0.326 ± 0.019	0.307 ± 0.019	0.225 ± 0.015	0.204 ± 0.012
0.69	0.343 ± 0.023	0.289 ± 0.019	0.230 ± 0.020	0.207 ± 0.015
0.81	0.366 ± 0.032	0.339 ± 0.034	0.222 ± 0.028	0.251 ± 0.025
0.94	0.386 ± 0.062	0.398 ± 0.060	0.315 ± 0.060	0.400 ± 0.057

are corrected for the currently accepted branching ratio of 0.692 for the  $K_S^0 \rightarrow \pi^+\pi^-$  decay mode [1]. For the major part of the spectra, our data are in agreement with the existing measurements within the error bars. Some small disagreements among the three data sets could be also because of the difference in beam momentum. The curves in the figure are the Legendre polynomial fits of

our  $K^-p \rightarrow \bar{K}^0n$  data,

$$d\sigma/d\Omega = \sum_{l=0}^{l_{\max}} A_l P_l(\cos \theta^*), \quad (4)$$

where  $P_l$  is the Legendre polynomial of order  $l$ , and  $A_l$  is its coefficient. The maximum order  $l_{\max}$  was chosen to provide a good fit to the data for each of the eight momenta. This choice results sometimes, especially for the lower beam momenta, in the higher-order coefficients



TABLE IV: Legendre polynomial coefficients for the  $K^-p \rightarrow \bar{K}^0n$  reaction for the four lowest beam momenta.

$p_{K^-} \pm \delta_p$ [MeV/c]	514 ± 10	560 ± 11	581 ± 12	629 ± 11
$A_0$	0.3071 ± 0.0092	0.3370 ± 0.0074	0.3242 ± 0.0070	0.3100 ± 0.0056
$A_1$	-0.023 ± 0.021	0.032 ± 0.017	0.028 ± 0.016	0.068 ± 0.014
$A_2$	0.247 ± 0.026	0.257 ± 0.023	0.250 ± 0.021	0.253 ± 0.018
$A_3$	-0.188 ± 0.031	-0.173 ± 0.027	-0.160 ± 0.025	-0.120 ± 0.021
$A_4$	0.008 ± 0.031	-0.004 ± 0.025	0.095 ± 0.023	0.092 ± 0.019
$A_5$	0.002 ± 0.034	0.021 ± 0.026	0.039 ± 0.025	0.036 ± 0.019
$\chi^2/\text{ndf}$	0.99	1.43	1.06	1.02

TABLE V: Legendre polynomial coefficients for the  $K^-p \rightarrow \bar{K}^0n$  reaction for the four highest beam momenta.

$p_{K^-} \pm \delta_p$ [MeV/c]	659 ± 12	687 ± 11	714 ± 11	750 ± 13
$A_0$	0.2774 ± 0.0055	0.2643 ± 0.0054	0.2241 ± 0.0049	0.1912 ± 0.0042
$A_1$	0.023 ± 0.013	0.008 ± 0.013	-0.057 ± 0.012	0.021 ± 0.011
$A_2$	0.208 ± 0.018	0.207 ± 0.018	0.194 ± 0.016	0.170 ± 0.014
$A_3$	-0.180 ± 0.020	-0.161 ± 0.020	-0.160 ± 0.019	-0.111 ± 0.016
$A_4$	0.072 ± 0.018	0.088 ± 0.018	0.090 ± 0.016	0.086 ± 0.013
$A_5$	0.0003 ± 0.0179	0.018 ± 0.018	-0.025 ± 0.016	0.019 ± 0.012
$\chi^2/\text{ndf}$	0.50	1.48	0.63	1.92

being consistent with zero. The results of Legendre polynomial fits for  $K^-p \rightarrow \bar{K}^0n$  are given for each of the eight beam momenta in Tables IV and V.

Our differential cross sections for  $K^-p \rightarrow \pi^0\Lambda$  as a function of  $\cos(\theta^*)$  for  $\pi^0$  are given for each of the eight beam momenta in Tables VI and VII. Our differential cross sections for  $K^-p \rightarrow \pi^0\Lambda$  are compared in Fig. 8 to the results of Armenteros [2] for similar beam momenta. The results of Armenteros are corrected for the currently accepted branching ratio of 0.639 for the  $\Lambda \rightarrow \pi^-p$  decay mode [1]. For the major part of the spectra, our data are in agreement with the results of Armenteros within the error bars. Note that our data have much smaller statistical uncertainties. Similar to the  $K^-p \rightarrow \bar{K}^0n$  results, some disagreement between the data could come from the difference between our beam momenta and those of Armenteros. Also, there could be some  $K^-p \rightarrow \pi^0\Sigma^0$  background in the data from Armenteros, especially in the backward  $\theta^*$  angles where the background reaction has a larger yield. The curves in the figure are the Legendre polynomial fits of our  $K^-p \rightarrow \pi^0\Lambda$  data. The fit results are given for each of the eight beam momenta in Tables VIII and IX.

Our differential cross sections for  $K^-p \rightarrow \pi^0\Sigma^0$  as a function of  $\cos(\theta^*)$  for  $\pi^0$  are given for each of the eight beam momenta in Tables X and XI. Our differential cross sections for  $K^-p \rightarrow \pi^0\Sigma^0$  are compared in Fig. 9 to the results of Armenteros [2] for similar beam momenta and also to the results of an independent analysis of the same data set reported recently in Ref. [10]. The results of Armenteros are corrected for the currently accepted branching ratio 0.639 of the  $\Lambda \rightarrow \pi^-p$  decay mode [1]. The curves in the figure are the Legendre polynomial fits of our  $K^-p \rightarrow \pi^0\Sigma^0$  data. The fit results are given

for each of the eight beam momenta in Tables XII and XIII. Note that our data are in reasonable agreement with the data from Armenteros within the error bars, but the quality and statistics of our data are much better. The measurement of  $K^-p \rightarrow \pi^0\Sigma^0$  by Armenteros [2] was conducted using a bubble-chamber set-up, in which the two photons from the  $\pi^0$  decay and the photon from the  $\Sigma^0$  decay were not detected. This resulted in a poorer  $\theta^*$  resolution and in a significant background from the  $\pi^0\pi^0\Lambda$  and  $\pi^0\pi^0\Sigma^0$  final states, especially for the highest momenta where the yield of these background reactions becomes large.

We note that some of our  $K^-p \rightarrow \pi^0\Sigma^0$  results, particularly for the forward production angles, are in disagreement with a separate analysis [10] of the same data by the Valparaiso-Argonne (VA) group of the Crystal Ball collaboration at the AGS. The results presented in our paper are obtained by the UCLA group, several members of which disagreed with the VA analysis and are not in the authors of Ref. [10]. There are several major differences between the two analyses that could lead to the disagreement observed in the  $K^-p \rightarrow \pi^0\Sigma^0$  results. First, we used the full fiducial volume of the CB in our analysis. This required a fine tuning of the MC simulation to reproduce the experimental conditions, including the CB energy trigger. The reduced fiducial volume, which is less sensitive to the MC simulation, was used in the VA analysis. However, this led to much less data and large uncertainties, especially for the forward direction where the largest discrepancy between the two analyses was observed. Second, the mean values of the beam-momentum spectra that were reconstructed by us for  $K^-p$  interactions in the LH<sub>2</sub> target [7, 12] were used in the VA analysis as nominal beam momenta. The nom-

TABLE VI: Differential cross sections for the  $K^- p \rightarrow \pi^0 \Lambda$  reaction for the four lowest beam momenta.

$p_{K^-} \pm \delta_p$ [MeV/c]	514 ± 10	560 ± 11	581 ± 12	629 ± 11
$\cos \theta^*(\pi^0)$	$d\sigma/d\Omega$ [mb/sr]	$d\sigma/d\Omega$ [mb/sr]	$d\sigma/d\Omega$ [mb/sr]	$d\sigma/d\Omega$ [mb/sr]
-0.94	0.076 ± 0.031	0.092 ± 0.024	0.118 ± 0.028	0.167 ± 0.016
-0.81	0.086 ± 0.012	0.123 ± 0.010	0.132 ± 0.011	0.180 ± 0.008
-0.69	0.078 ± 0.011	0.130 ± 0.009	0.141 ± 0.008	0.174 ± 0.007
-0.56	0.100 ± 0.010	0.138 ± 0.008	0.153 ± 0.008	0.188 ± 0.007
-0.44	0.098 ± 0.009	0.122 ± 0.008	0.143 ± 0.008	0.163 ± 0.006
-0.31	0.118 ± 0.010	0.128 ± 0.008	0.136 ± 0.007	0.151 ± 0.006
-0.19	0.112 ± 0.010	0.115 ± 0.008	0.126 ± 0.007	0.144 ± 0.006
-0.06	0.119 ± 0.010	0.125 ± 0.008	0.128 ± 0.007	0.126 ± 0.006
0.06	0.134 ± 0.012	0.143 ± 0.008	0.149 ± 0.008	0.129 ± 0.006
0.19	0.178 ± 0.013	0.179 ± 0.009	0.176 ± 0.008	0.140 ± 0.006
0.31	0.206 ± 0.014	0.211 ± 0.010	0.202 ± 0.009	0.164 ± 0.006
0.44	0.288 ± 0.017	0.241 ± 0.011	0.265 ± 0.010	0.199 ± 0.007
0.56	0.357 ± 0.018	0.345 ± 0.014	0.315 ± 0.012	0.245 ± 0.009
0.69	0.421 ± 0.023	0.379 ± 0.018	0.373 ± 0.014	0.334 ± 0.011
0.81	0.531 ± 0.039	0.477 ± 0.028	0.410 ± 0.027	0.414 ± 0.020
0.94	0.737 ± 0.145	0.675 ± 0.135	0.686 ± 0.113	0.817 ± 0.150

TABLE VII: Differential cross sections for the  $K^- p \rightarrow \pi^0 \Lambda$  reaction for the four highest beam momenta.

$p_{K^-} \pm \delta_p$ [MeV/c]	659 ± 12	687 ± 11	714 ± 11	750 ± 13
$\cos \theta^*(\pi^0)$	$d\sigma/d\Omega$ [mb/sr]	$d\sigma/d\Omega$ [mb/sr]	$d\sigma/d\Omega$ [mb/sr]	$d\sigma/d\Omega$ [mb/sr]
-0.94	0.162 ± 0.016	0.228 ± 0.021	0.307 ± 0.017	0.452 ± 0.016
-0.81	0.209 ± 0.009	0.262 ± 0.010	0.308 ± 0.009	0.372 ± 0.008
-0.69	0.226 ± 0.008	0.268 ± 0.009	0.300 ± 0.008	0.288 ± 0.007
-0.56	0.214 ± 0.008	0.252 ± 0.008	0.254 ± 0.007	0.253 ± 0.006
-0.44	0.183 ± 0.006	0.221 ± 0.007	0.202 ± 0.007	0.206 ± 0.005
-0.31	0.168 ± 0.006	0.189 ± 0.007	0.185 ± 0.006	0.156 ± 0.005
-0.19	0.140 ± 0.006	0.157 ± 0.006	0.142 ± 0.005	0.127 ± 0.004
-0.06	0.125 ± 0.005	0.130 ± 0.005	0.127 ± 0.005	0.105 ± 0.004
0.06	0.131 ± 0.005	0.114 ± 0.005	0.104 ± 0.005	0.087 ± 0.004
0.19	0.131 ± 0.005	0.116 ± 0.005	0.102 ± 0.005	0.079 ± 0.003
0.31	0.149 ± 0.006	0.128 ± 0.006	0.115 ± 0.005	0.100 ± 0.004
0.44	0.182 ± 0.007	0.168 ± 0.007	0.154 ± 0.006	0.138 ± 0.005
0.56	0.239 ± 0.008	0.214 ± 0.008	0.200 ± 0.007	0.216 ± 0.006
0.69	0.306 ± 0.011	0.317 ± 0.011	0.298 ± 0.011	0.327 ± 0.009
0.81	0.461 ± 0.023	0.457 ± 0.026	0.514 ± 0.028	0.526 ± 0.026
0.94	0.67 ± 0.28	—	—	—

TABLE VIII: Legendre polynomial coefficients for the  $K^- p \rightarrow \pi^0 \Lambda$  reaction for the four lowest beam momenta.

$p_{K^-} \pm \delta_p$ [MeV/c]	514 ± 10	560 ± 11	581 ± 12	629 ± 11
$A_0$	0.2240 ± 0.0065	0.2195 ± 0.0050	0.2160 ± 0.0046	0.2171 ± 0.0036
$A_1$	0.274 ± 0.015	0.208 ± 0.011	0.178 ± 0.010	0.1367 ± 0.0084
$A_2$	0.180 ± 0.022	0.148 ± 0.017	0.120 ± 0.016	0.172 ± 0.012
$A_3$	0.075 ± 0.019	0.056 ± 0.014	0.044 ± 0.013	0.098 ± 0.010
$A_4$	-0.004 ± 0.019	-0.031 ± 0.015	-0.047 ± 0.014	-0.052 ± 0.011
$\chi^2/\text{ndf}$	0.65	0.94	0.75	0.93

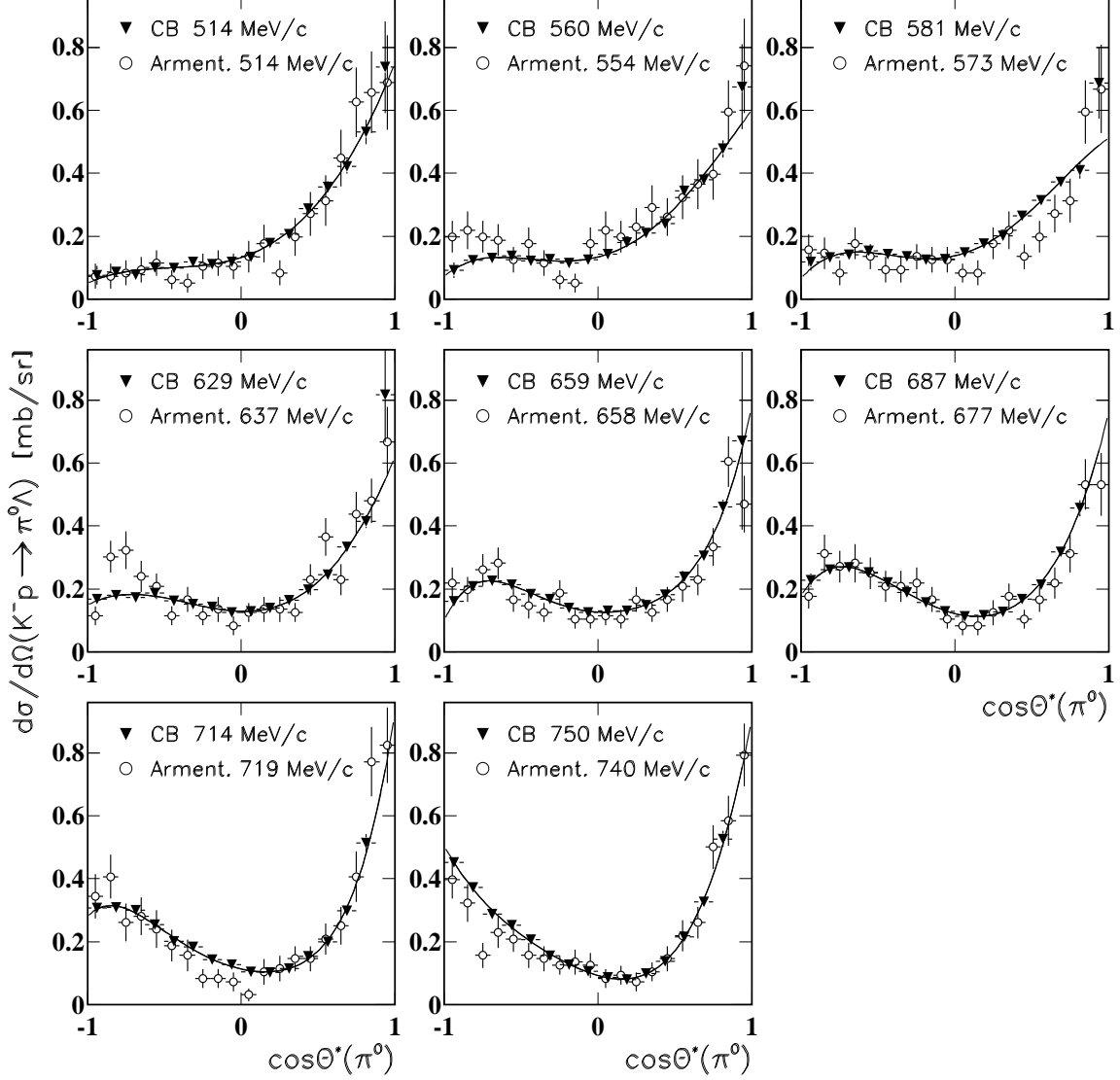


FIG. 8: Our differential cross sections for  $K^-p \rightarrow \pi^0\Lambda$  compared to the results of Armenteros [2] for similar beam momenta. The curves are the Legendre polynomial fits of our data.

TABLE IX: Legendre polynomial coefficients for the  $K^-p \rightarrow \pi^0\Lambda$  reaction for the four highest beam momenta.

$p_{K^-} \pm \delta_p$ [MeV/c]	$659 \pm 12$	$687 \pm 11$	$714 \pm 11$	$750 \pm 13$
$A_0$	$0.2291 \pm 0.0045$	$0.2411 \pm 0.0049$	$0.2527 \pm 0.0051$	$0.2619 \pm 0.0044$
$A_1$	$0.138 \pm 0.012$	$0.098 \pm 0.014$	$0.094 \pm 0.014$	$0.067 \pm 0.013$
$A_2$	$0.208 \pm 0.016$	$0.235 \pm 0.018$	$0.310 \pm 0.018$	$0.383 \pm 0.016$
$A_3$	$0.161 \pm 0.018$	$0.172 \pm 0.021$	$0.188 \pm 0.020$	$0.135 \pm 0.018$
$A_4$	$0.004 \pm 0.014$	$-0.004 \pm 0.014$	$0.041 \pm 0.014$	$0.060 \pm 0.012$
$A_5$	$0.041 \pm 0.013$	$0.021 \pm 0.014$	$0.042 \pm 0.013$	$-0.0003 \pm 0.0111$
$\chi^2/\text{ndf}$	0.52	0.29	1.60	1.15

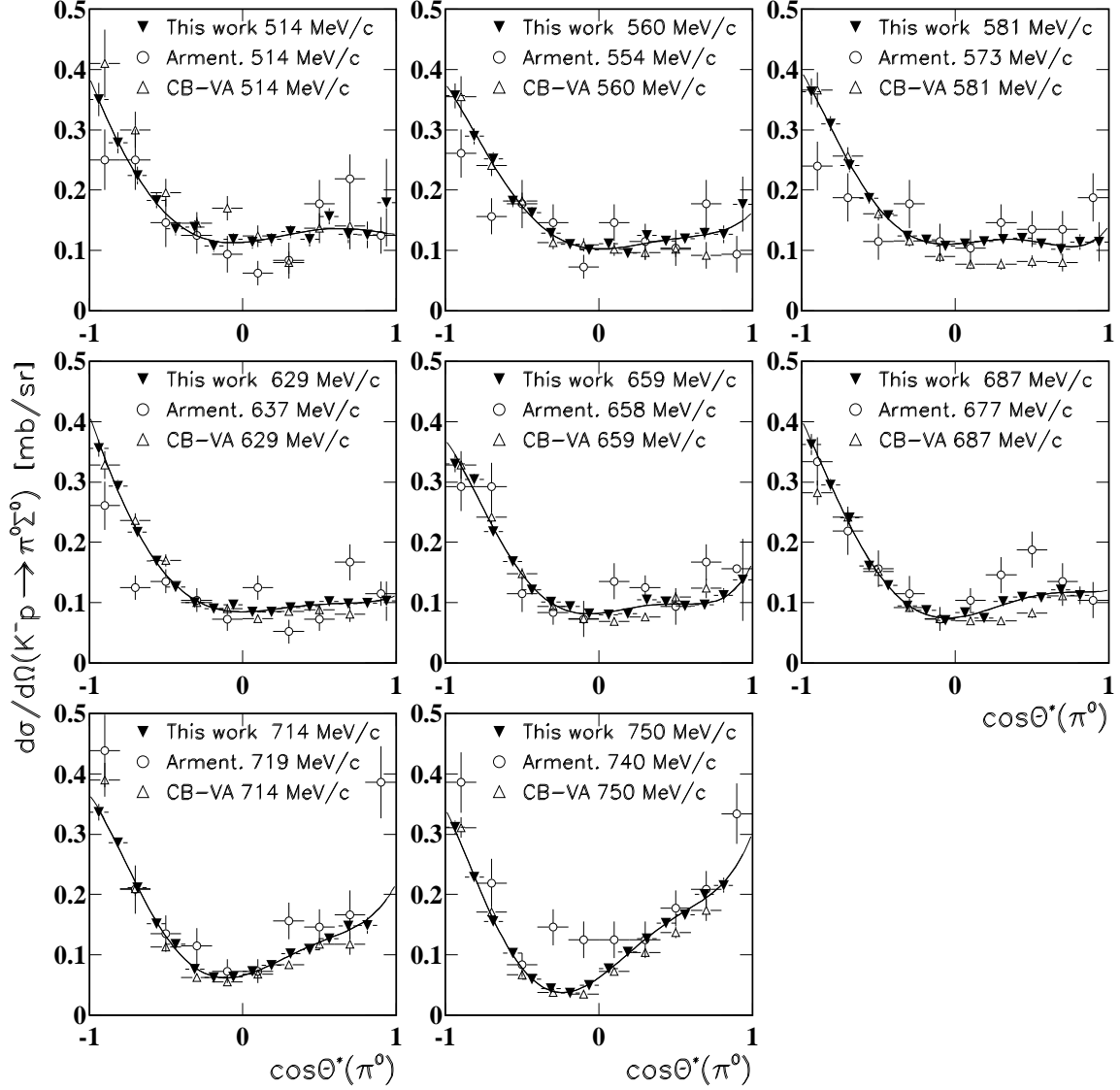


FIG. 9: Our differential cross sections for  $K^-p \rightarrow \pi^0\Sigma^0$  compared to the results of Armenteros [2] for similar beam momenta and to the VA results [10]. The curves are the Legendre polynomial fits of our data.

inal momenta are used as the input for the transport matrix of the dipole magnet in order to calculate the momentum of an individual beam particle based on the information of the drift chambers that were located upstream and downstream of the magnet. Because of the energy losses in the beam counters, there is a difference between the beam momenta in the magnet and in the target. The use of the incorrect beam-momentum information in the event reconstruction usually leads to some distortion of the final angular distributions in the c.m. system. Third, our analysis showed good agreement with the older measurements of  $K^-p \rightarrow \bar{K}^0n$  and  $K^-p \rightarrow \pi^0\Lambda$ , the quality of which is much better than the old  $K^-p \rightarrow \pi^0\Sigma^0$  data. These measurements are also needed for the accurate subtraction of background contributions from the  $K^-p \rightarrow \pi^0\Sigma^0$  candidates. The background subtraction in the VA analysis is less accurate as

it relies on the Armenteros data [2], which were obtained often for different beam momenta, with poor statistics, and without background subtraction. The same is for the subtraction of the  $K^-p \rightarrow \pi^0\pi^0\Lambda$  background; the poor Armenteros data [2] were used in the VA analysis instead of the results obtained for this reaction in the same experiment [7]. Another difference between the two analyses is that we used the kinematic-fit technique as part of the event reconstruction. This provided a better experimental resolution in  $\theta^*$  and allows to use the fit C.L. for the event selection.

Our evaluation of the total cross sections for reactions  $K^-p \rightarrow \bar{K}^0n$ ,  $K^-p \rightarrow \pi^0\Lambda$ , and  $K^-p \rightarrow \pi^0\Sigma^0$  was based on the Legendre polynomial fit of the corresponding differential cross sections; the results obtained are listed for each of the eight beam momenta in Table XIV. Since the results of our fits vary slightly depending on the maxi-

TABLE X: Differential cross sections for the  $K^-p \rightarrow \pi^0\Sigma^0$  reaction for the four lowest beam momenta.

$p_{K^-} \pm \delta_p$ [MeV/c]	514 ± 10	560 ± 11	581 ± 12	629 ± 11
$\cos \theta^*(\pi^0)$	$d\sigma/d\Omega$ [mb/sr]	$d\sigma/d\Omega$ [mb/sr]	$d\sigma/d\Omega$ [mb/sr]	$d\sigma/d\Omega$ [mb/sr]
-0.94	0.350 ± 0.028	0.356 ± 0.021	0.363 ± 0.021	0.356 ± 0.014
-0.81	0.278 ± 0.017	0.289 ± 0.013	0.310 ± 0.012	0.294 ± 0.010
-0.69	0.224 ± 0.015	0.252 ± 0.011	0.241 ± 0.011	0.217 ± 0.008
-0.56	0.183 ± 0.013	0.182 ± 0.010	0.187 ± 0.010	0.169 ± 0.007
-0.44	0.136 ± 0.011	0.162 ± 0.009	0.159 ± 0.008	0.126 ± 0.006
-0.31	0.139 ± 0.011	0.128 ± 0.008	0.124 ± 0.008	0.100 ± 0.006
-0.19	0.108 ± 0.010	0.110 ± 0.008	0.118 ± 0.007	0.091 ± 0.005
-0.06	0.119 ± 0.010	0.101 ± 0.007	0.108 ± 0.007	0.096 ± 0.005
0.06	0.114 ± 0.010	0.111 ± 0.007	0.111 ± 0.006	0.085 ± 0.005
0.19	0.118 ± 0.010	0.096 ± 0.007	0.115 ± 0.006	0.084 ± 0.005
0.31	0.131 ± 0.011	0.125 ± 0.008	0.119 ± 0.007	0.092 ± 0.005
0.44	0.119 ± 0.012	0.116 ± 0.008	0.121 ± 0.006	0.094 ± 0.005
0.56	0.157 ± 0.013	0.120 ± 0.008	0.111 ± 0.008	0.103 ± 0.006
0.69	0.127 ± 0.014	0.129 ± 0.010	0.102 ± 0.010	0.099 ± 0.007
0.81	0.126 ± 0.022	0.127 ± 0.014	0.114 ± 0.013	0.099 ± 0.010
0.94	0.179 ± 0.073	0.177 ± 0.045	0.114 ± 0.033	0.103 ± 0.033

TABLE XI: Differential cross sections for the  $K^-p \rightarrow \pi^0\Sigma^0$  reaction for the four highest beam momenta.

$p_{K^-} \pm \delta_p$ [MeV/c]	659 ± 12	687 ± 11	714 ± 11	750 ± 13
$\cos \theta^*(\pi^0)$	$d\sigma/d\Omega$ [mb/sr]	$d\sigma/d\Omega$ [mb/sr]	$d\sigma/d\Omega$ [mb/sr]	$d\sigma/d\Omega$ [mb/sr]
-0.94	0.330 ± 0.014	0.362 ± 0.017	0.337 ± 0.014	0.312 ± 0.011
-0.81	0.304 ± 0.009	0.295 ± 0.010	0.286 ± 0.009	0.229 ± 0.006
-0.69	0.218 ± 0.008	0.241 ± 0.008	0.211 ± 0.007	0.155 ± 0.005
-0.56	0.168 ± 0.007	0.161 ± 0.007	0.152 ± 0.006	0.103 ± 0.004
-0.44	0.121 ± 0.006	0.129 ± 0.005	0.118 ± 0.005	0.060 ± 0.003
-0.31	0.101 ± 0.005	0.095 ± 0.005	0.076 ± 0.004	0.044 ± 0.003
-0.19	0.094 ± 0.005	0.087 ± 0.005	0.062 ± 0.004	0.037 ± 0.003
-0.06	0.082 ± 0.005	0.070 ± 0.004	0.064 ± 0.004	0.049 ± 0.003
0.06	0.080 ± 0.005	0.083 ± 0.005	0.073 ± 0.004	0.077 ± 0.003
0.19	0.082 ± 0.005	0.075 ± 0.005	0.083 ± 0.004	0.105 ± 0.004
0.31	0.105 ± 0.005	0.102 ± 0.006	0.102 ± 0.005	0.127 ± 0.004
0.44	0.101 ± 0.005	0.109 ± 0.006	0.109 ± 0.005	0.153 ± 0.005
0.56	0.095 ± 0.005	0.108 ± 0.006	0.127 ± 0.006	0.166 ± 0.005
0.69	0.097 ± 0.007	0.122 ± 0.007	0.148 ± 0.007	0.200 ± 0.007
0.81	0.112 ± 0.012	0.112 ± 0.015	0.149 ± 0.013	0.215 ± 0.013
0.94	0.138 ± 0.068	—	—	—

imum polynomial order used, there could be a small difference between our values for the total cross sections and the results of any independent analysis of our differential cross sections. The uncertainties that we give to our total cross sections are based only on the statistical uncertainties in the points of the differential cross sections themselves. This leads to a smaller uncertainty of the total cross sections obtained from the differential cross sections in which the point  $\cos(\theta^*) = 0.94$  is omitted. The systematic uncertainty of 7% in the differential cross

sections is not included in the error calculation. Our values for the total cross sections of the three reactions are compared in Fig. 10 to the results from Armenteros [2], Alston-Garnjost [3], and London [5]. There is no comparison to the  $K^-p \rightarrow \pi^0\Sigma^0$  total cross sections from the VA analysis as their values are not reported in Ref. [10]. As shown, our total cross sections for  $K^-p \rightarrow \bar{K}^0n$  within the error bars are in agreement with the existing data. Our total cross sections for  $K^-p \rightarrow \pi^0\Lambda$  are in a better agreement with the data from Armenteros than with

TABLE XII: Legendre polynomial coefficients for the  $K^-p \rightarrow \pi^0\Sigma^0$  reaction for the four lowest beam momenta.

$p_{K^-} \pm \delta_p$ [MeV/c]	514 ± 10	560 ± 11	581 ± 12	629 ± 11
$A_0$	0.1603 ± 0.0049	0.1598 ± 0.0034	0.1582 ± 0.0030	0.1387 ± 0.0023
$A_1$	-0.079 ± 0.013	-0.0874 ± 0.0086	-0.1026 ± 0.0076	-0.1009 ± 0.0060
$A_2$	0.095 ± 0.017	0.112 ± 0.011	0.1010 ± 0.0097	0.1141 ± 0.0077
$A_3$	-0.058 ± 0.020	-0.035 ± 0.014	-0.049 ± 0.012	-0.0571 ± 0.0095
$A_4$	0.002 ± 0.017	-0.002 ± 0.011	0.009 ± 0.010	0.0089 ± 0.0079
$A_5$	0.006 ± 0.018	0.016 ± 0.012	0.024 ± 0.011	0.0083 ± 0.0088
$\chi^2/\text{ndf}$	0.85	1.03	0.27	0.82

TABLE XIII: Legendre polynomial coefficients for the  $K^-p \rightarrow \pi^0\Sigma^0$  reaction for the four highest beam momenta.

$p_{K^-} \pm \delta_p$ [MeV/c]	659 ± 12	687 ± 11	714 ± 11	750 ± 13
$A_0$	0.1397 ± 0.0027	0.1426 ± 0.0033	0.1437 ± 0.0030	0.1439 ± 0.0027
$A_1$	-0.0897 ± 0.0073	-0.0939 ± 0.0092	-0.0547 ± 0.0083	0.0185 ± 0.0074
$A_2$	0.1202 ± 0.0095	0.128 ± 0.012	0.153 ± 0.011	0.1693 ± 0.0095
$A_3$	-0.041 ± 0.012	-0.061 ± 0.014	-0.046 ± 0.013	-0.069 ± 0.011
$A_4$	0.0076 ± 0.0089	-0.009 ± 0.010	-0.0044 ± 0.0094	0.0085 ± 0.0081
$A_5$	0.0286 ± 0.0095	0.014 ± 0.011	0.0270 ± 0.0095	0.0313 ± 0.0078
$\chi^2/\text{ndf}$	1.79	1.95	0.89	0.96

the ones from London, where our results have the smallest statistical uncertainties. Our total cross sections for  $K^-p \rightarrow \pi^0\Sigma^0$  also have the smallest statistical uncertainties and lie somewhere between the results from Armenteros and London.

The induced polarization of the  $\Lambda$  hyperon in the  $K^-p \rightarrow \pi^0\Lambda$  reaction was measured via its decay asymmetry:

$$P_\Lambda(\cos\theta^*) = 3\left(\sum_i \cos\xi_i\right)/(\alpha_\Lambda N(\theta^*)) , \quad (5)$$

where  $\theta^*$  is the angle between the direction of the outgoing  $\pi^0$  and the incident  $K^-$  in the c.m. system. The  $\xi$  angle is defined by

$$\cos\xi = (\hat{\mathbf{K}}^- \times \hat{\boldsymbol{\pi}}^0) \cdot \hat{\mathbf{n}} / |\hat{\mathbf{K}}^- \times \hat{\boldsymbol{\pi}}^0| = \hat{\mathbf{N}} \cdot \hat{\mathbf{n}} , \quad (6)$$

where  $\hat{\mathbf{K}}^-$  and  $\hat{\boldsymbol{\pi}}^0$  are unit vectors in the direction of the incident  $K^-$  and the outgoing  $\pi^0$  meson respectively,  $\hat{\mathbf{n}}$  is a unit vector in the direction of the decay neutron in the  $\Lambda$  rest frame,  $\hat{\mathbf{N}}$  is the normal to the production plane.  $N(\theta^*)$  is the total number of  $\Lambda$  hyperons produced at the angle  $\theta^*$ , and  $\alpha_\Lambda = +0.65$  is the asymmetry parameter for  $\Lambda \rightarrow \pi^0n$ .

Our results for the  $\Lambda$  polarization as a function of  $\cos\theta^*(\pi^0)$  for the  $K^-p \rightarrow \pi^0\Lambda$  reaction are given for each of the eight beam momenta in Tables XV and XVI. These results are also shown in Fig. 11. The comparison of our results for the product of the  $\Lambda$  polarization and the differential cross section of  $K^-p \rightarrow \pi^0\Lambda$  with the data from Armenteros[2] is shown in Fig. 12. Both the results are in agreement within the error bars, where our statistical uncertainties are much smaller. The curves in

the figure are the fits of our  $K^-p \rightarrow \pi^0\Lambda$  data to the first associated Legendre functions,

$$P(d\sigma/d\Omega) = \sum_{l=0}^{l_{\max}} B_l P_l^1(\cos\theta^*) . \quad (7)$$

The results of the fits are given for each of the eight beam momenta in Tables XVII and XVIII.

The induced polarization of the  $\Sigma^0$  hyperon in the  $K^-p \rightarrow \pi^0\Sigma^0$  reaction was measured via its decay asymmetry (see Ref. [15]):

$$P_{\Sigma^0}(\cos\theta^*) = -9\left(\sum_i \cos\xi_i \cos\psi_i\right)/(\alpha_\Lambda N(\theta^*)) , \quad (8)$$

where  $\theta^*$  is the angle between the direction of the outgoing  $\pi^0$  and the incident  $K^-$  in the c.m. system. The  $\xi$  angle was defined by

$$\cos\xi = (\hat{\mathbf{K}}^- \times \hat{\boldsymbol{\Sigma}}^0) \cdot \hat{\boldsymbol{\Lambda}} / |\hat{\mathbf{K}}^- \times \hat{\boldsymbol{\Sigma}}^0| = \hat{\mathbf{N}} \cdot \hat{\boldsymbol{\Lambda}} , \quad (9)$$

where  $\hat{\mathbf{K}}^-$  and  $\hat{\boldsymbol{\Sigma}}^0$  are unit vectors in the direction of the incident  $K^-$  and the outgoing  $\Sigma^0$  hyperon, respectively.  $\hat{\boldsymbol{\Lambda}}$  is a unit vector in the direction of the  $\Lambda$  hyperon in the  $\Sigma^0$  rest frame,  $\hat{\mathbf{N}}$  is the normal to the production plane. The  $\psi$  angle was defined by

$$\cos\psi = \hat{\boldsymbol{\Lambda}} \cdot \hat{\mathbf{n}} , \quad (10)$$

where  $\hat{\mathbf{n}}$  is a unit vector in the direction of the decay neutron in the  $\Lambda$  rest frame.  $N(\theta^*)$  is the total number of the  $\Sigma^0$  hyperons produced at the angle  $\theta^*$ , and  $\alpha_\Lambda = +0.65$  is the asymmetry parameter for  $\Lambda \rightarrow \pi^0n$ . The

TABLE XIV: The total cross sections for reactions  $K^-p \rightarrow \bar{K}^0 n$ ,  $K^-p \rightarrow \pi^0 \Lambda$ , and  $K^-p \rightarrow \pi^0 \Sigma^0$  at the eight beam momenta.

$p_{K^-} \pm \sigma_p$ [MeV/c]	514±10	560±11	581±12	629±11	659±12	687±11	714±11	750±13
$\sigma_{\bar{K}^0 n}$ [mb]	3.86 ± 0.12	4.23 ± 0.09	4.07 ± 0.09	3.89 ± 0.07	3.49 ± 0.07	3.32 ± 0.07	2.82 ± 0.07	2.40 ± 0.06
$\sigma_{\pi^0 \Lambda}$ [mb]	2.82 ± 0.12	2.76 ± 0.11	2.72 ± 0.09	2.73 ± 0.11	2.88 ± 0.22	3.03 ± 0.04	3.18 ± 0.04	3.29 ± 0.04
$\sigma_{\pi^0 \Sigma^0}$ [mb]	2.02 ± 0.07	2.01 ± 0.05	1.99 ± 0.04	1.74 ± 0.04	1.76 ± 0.06	1.79 ± 0.03	1.81 ± 0.03	1.81 ± 0.02

TABLE XV: Polarization of the  $\Lambda$  hyperon in the  $K^-p \rightarrow \pi^0 \Lambda$  reaction for the four lowest beam momenta.

$p_{K^-} \pm \delta_p$ [MeV/c]	514 ± 10	560 ± 11	581 ± 12	629 ± 11
$\cos \theta^*(\pi^0)$	$P_\Lambda$	$P_\Lambda$	$P_\Lambda$	$P_\Lambda$
-0.94	-0.08 ± 0.16	0.05 ± 0.12	0.02 ± 0.09	0.05 ± 0.09
-0.81	-0.16 ± 0.19	0.01 ± 0.13	-0.06 ± 0.10	0.18 ± 0.09
-0.69	-0.25 ± 0.22	-0.04 ± 0.13	0.18 ± 0.10	0.31 ± 0.09
-0.56	-0.28 ± 0.21	0.25 ± 0.13	0.00 ± 0.10	0.15 ± 0.08
-0.44	0.34 ± 0.20	-0.02 ± 0.13	0.13 ± 0.10	0.22 ± 0.09
-0.31	-0.40 ± 0.17	-0.01 ± 0.13	-0.06 ± 0.10	0.40 ± 0.09
-0.19	0.22 ± 0.18	0.04 ± 0.14	0.15 ± 0.11	0.25 ± 0.09
-0.06	0.20 ± 0.19	0.02 ± 0.13	0.36 ± 0.10	0.26 ± 0.10
0.06	0.28 ± 0.16	0.34 ± 0.12	0.22 ± 0.10	0.36 ± 0.10
0.19	0.10 ± 0.15	0.20 ± 0.11	0.12 ± 0.09	0.18 ± 0.09
0.31	0.11 ± 0.14	0.18 ± 0.10	0.46 ± 0.09	0.12 ± 0.09
0.44	0.03 ± 0.13	0.20 ± 0.10	0.09 ± 0.08	0.32 ± 0.08
0.56	0.38 ± 0.12	0.13 ± 0.09	0.20 ± 0.08	0.22 ± 0.08
0.69	0.26 ± 0.13	0.09 ± 0.09	0.26 ± 0.08	0.13 ± 0.08
0.81	0.15 ± 0.16	-0.08 ± 0.12	0.16 ± 0.11	0.13 ± 0.11
0.94	-0.05 ± 0.37	0.16 ± 0.36	0.00 ± 0.28	—

TABLE XVI: Polarization of the  $\Lambda$  hyperon in the  $K^-p \rightarrow \pi^0 \Lambda$  reaction for the four highest beam momenta.

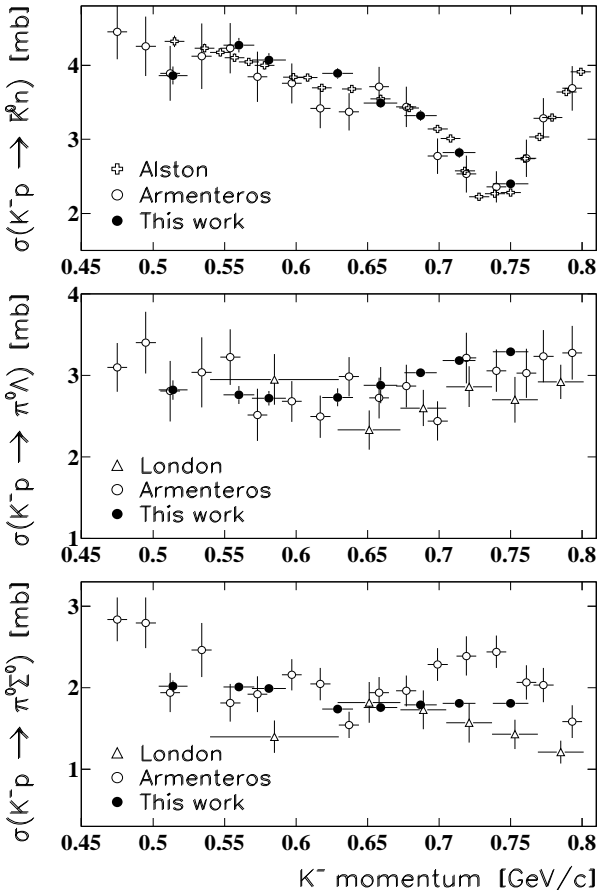
$p_{K^-} \pm \delta_p$ [MeV/c]	659 ± 12	687 ± 11	714 ± 11	750 ± 13
$\cos \theta^*(\pi^0)$	$P_\Lambda$	$P_\Lambda$	$P_\Lambda$	$P_\Lambda$
-0.94	0.28 ± 0.09	0.51 ± 0.08	0.44 ± 0.08	0.36 ± 0.05
-0.81	0.50 ± 0.07	0.41 ± 0.07	0.58 ± 0.06	0.54 ± 0.04
-0.69	0.40 ± 0.07	0.44 ± 0.06	0.57 ± 0.06	0.48 ± 0.05
-0.56	0.29 ± 0.07	0.30 ± 0.07	0.43 ± 0.06	0.38 ± 0.05
-0.44	0.27 ± 0.08	0.36 ± 0.07	0.23 ± 0.07	0.19 ± 0.06
-0.31	0.19 ± 0.08	0.26 ± 0.07	0.15 ± 0.07	0.06 ± 0.06
-0.19	0.32 ± 0.09	0.24 ± 0.08	-0.02 ± 0.08	-0.17 ± 0.07
-0.06	0.35 ± 0.09	0.24 ± 0.09	0.05 ± 0.08	-0.28 ± 0.07
0.06	0.13 ± 0.09	0.16 ± 0.09	-0.06 ± 0.09	-0.28 ± 0.08
0.19	0.33 ± 0.09	0.11 ± 0.09	-0.26 ± 0.09	-0.21 ± 0.08
0.31	0.33 ± 0.09	0.13 ± 0.09	-0.26 ± 0.09	-0.36 ± 0.07
0.44	0.08 ± 0.08	0.04 ± 0.08	-0.13 ± 0.08	-0.34 ± 0.06
0.56	0.11 ± 0.08	0.05 ± 0.08	-0.26 ± 0.07	-0.29 ± 0.06
0.69	-0.03 ± 0.08	-0.05 ± 0.08	-0.36 ± 0.08	-0.34 ± 0.06
0.81	0.00 ± 0.11	-0.24 ± 0.12	-0.26 ± 0.13	-0.33 ± 0.10
0.94	—	—	—	—

TABLE XVII: Associated Legendre function coefficients for the  $K^-p \rightarrow \pi^0\Lambda$  reaction for the four lowest beam momenta.

$p_{K^-} \pm \delta_p$ [MeV/c]	514 ± 10	560 ± 11	581 ± 12	629 ± 11
$B_1$	-0.0306 ± 0.0099	-0.0232 ± 0.0072	-0.0401 ± 0.0060	-0.0489 ± 0.0054
$B_2$	-0.0311 ± 0.0096	-0.0114 ± 0.0067	-0.0223 ± 0.0055	-0.0051 ± 0.0051
$B_3$	-0.0096 ± 0.0081	0.0004 ± 0.0058	-0.0062 ± 0.0047	-0.0093 ± 0.0043
$B_4$	-0.0034 ± 0.0051	0.0044 ± 0.0040	-0.0004 ± 0.0034	-0.0052 ± 0.0035
$\chi^2/\text{ndf}$	1.40	0.69	1.61	1.30

TABLE XVIII: Associated Legendre function coefficients for the  $K^-p \rightarrow \pi^0\Lambda$  reaction for the four highest beam momenta.

$p_{K^-} \pm \delta_p$ [MeV/c]	659 ± 12	687 ± 11	714 ± 11	750 ± 13
$B_1$	-0.0435 ± 0.0054	-0.0415 ± 0.0055	-0.0111 ± 0.0053	0.0038 ± 0.0043
$B_2$	0.0249 ± 0.0058	0.0407 ± 0.0060	0.0750 ± 0.0059	0.0785 ± 0.0048
$B_3$	-0.0030 ± 0.0052	-0.0099 ± 0.0055	-0.0110 ± 0.0056	-0.0124 ± 0.0048
$B_4$	0.0109 ± 0.0043	0.0112 ± 0.0043	0.0251 ± 0.0042	0.0312 ± 0.0033
$B_5$	0.0030 ± 0.0033	0.0017 ± 0.0035	0.0035 ± 0.0036	0.0019 ± 0.0029
$\chi^2/\text{ndf}$	1.18	0.61	0.97	0.57

FIG. 10: Our total cross sections for  $K^-p \rightarrow \bar{K}^0n$ ,  $K^-p \rightarrow \pi^0\Lambda$ , and  $K^-p \rightarrow \pi^0\Sigma^0$  compared to the results from Armenteros [2], Alston-Garnjost [3], and London [5].

measured values for the  $\Sigma^0$  polarization were corrected for the  $\cos \xi$  acceptance, which turned out to be about 30% smaller for the central  $\cos \xi$  values. (see Ref. [10] for more details).

Our results for the  $\Sigma^0$  polarization as a function of  $\cos \theta^*(\pi^0)$  for the  $K^-p \rightarrow \pi^0\Sigma^0$  reaction are given for each of the eight beam momenta in Tables XIX and XX. These results are also shown in Fig. 13, compared to the VA analysis [10]. As seen, our results have smaller statistical uncertainties. Our sign for the polarization is opposite to the one from the VA analysis. Also, our magnitudes for the polarization at the lowest beam momenta are systematically smaller for the forward angles, in which the VA data have much smaller acceptance. We were not able to get any analysis details from the authors of Ref. [10] that would help us to explain the difference between the two sets of results. We want only to note that a similar measurement of the  $\Lambda$  polarization gave us reasonable agreement with the data from Armenteros.

The comparison of our results for the product of the  $\Sigma^0$  polarization and the differential cross section of  $K^-p \rightarrow \pi^0\Sigma^0$  with the data from Armenteros[2] is shown Fig. 12. The results from Armenteros have very large statistical uncertainties. Also, the quality of the data from Armenteros is poorer, as they could not measure  $\Sigma^0$  and  $\pi^0$  directly. The large uncertainties of the data from Armenteros do not allow the comparison of their sign of the  $\Sigma^0$  polarization with ours. The curves in the figure are the fits of our  $K^-p \rightarrow \pi^0\Sigma^0$  data to the first associated Legendre functions. The results of the fits are given for each of the eight beam momenta in Tables XXI and XXII.



TABLE XIX: Polarization of the  $\Sigma^0$  hyperon in the  $K^-p \rightarrow \pi^0\Sigma^0$  reaction for the four lowest beam momenta.

$p_{K^-} \pm \delta_p$ [MeV/c]	514 $\pm$ 10	560 $\pm$ 11	581 $\pm$ 12	629 $\pm$ 11
$\cos \theta^*(\pi^0)$	$P_{\Sigma^0}$	$P_{\Sigma^0}$	$P_{\Sigma^0}$	$P_{\Sigma^0}$
-0.94	0.14 $\pm$ 0.25	-0.28 $\pm$ 0.17	-0.14 $\pm$ 0.14	0.18 $\pm$ 0.15
-0.81	0.32 $\pm$ 0.24	-0.33 $\pm$ 0.17	-0.10 $\pm$ 0.14	-0.16 $\pm$ 0.13
-0.69	-0.56 $\pm$ 0.24	-0.09 $\pm$ 0.19	-0.31 $\pm$ 0.15	-0.11 $\pm$ 0.15
-0.56	-0.77 $\pm$ 0.27	-0.38 $\pm$ 0.19	-0.28 $\pm$ 0.16	-0.37 $\pm$ 0.16
-0.44	-0.50 $\pm$ 0.35	-0.69 $\pm$ 0.20	-0.35 $\pm$ 0.18	-0.37 $\pm$ 0.18
-0.31	-0.39 $\pm$ 0.28	-0.38 $\pm$ 0.22	-0.27 $\pm$ 0.20	-0.30 $\pm$ 0.19
-0.19	-0.96 $\pm$ 0.31	-0.53 $\pm$ 0.26	-0.21 $\pm$ 0.19	-0.18 $\pm$ 0.21
-0.06	-0.77 $\pm$ 0.32	-0.99 $\pm$ 0.26	-0.59 $\pm$ 0.20	-0.41 $\pm$ 0.21
0.06	-1.02 $\pm$ 0.32	-0.75 $\pm$ 0.26	-0.71 $\pm$ 0.20	-0.31 $\pm$ 0.21
0.19	-0.75 $\pm$ 0.34	-1.38 $\pm$ 0.29	-0.73 $\pm$ 0.21	-0.43 $\pm$ 0.22
0.31	-0.16 $\pm$ 0.30	-0.62 $\pm$ 0.24	-0.69 $\pm$ 0.21	-0.81 $\pm$ 0.21
0.44	-1.37 $\pm$ 0.37	-0.52 $\pm$ 0.25	-0.44 $\pm$ 0.21	-0.53 $\pm$ 0.21
0.56	-0.37 $\pm$ 0.32	-0.43 $\pm$ 0.28	-0.87 $\pm$ 0.21	-0.37 $\pm$ 0.23
0.69	-0.14 $\pm$ 0.41	-0.82 $\pm$ 0.31	-0.50 $\pm$ 0.26	-0.71 $\pm$ 0.25
0.81	-0.84 $\pm$ 0.47	-1.20 $\pm$ 0.43	-0.38 $\pm$ 0.39	0.32 $\pm$ 0.36
0.94	-2.22 $\pm$ 0.84	-0.75 $\pm$ 1.00	1.99 $\pm$ 0.95	-0.82 $\pm$ 0.69

TABLE XX: Polarization of the  $\Sigma^0$  hyperon in the  $K^-p \rightarrow \pi^0\Sigma^0$  reaction for the four highest beam momenta.

$p_{K^-} \pm \delta_p$ [MeV/c]	659 $\pm$ 12	687 $\pm$ 11	714 $\pm$ 11	750 $\pm$ 13
$\cos \theta^*(\pi^0)$	$P_{\Sigma^0}$	$P_{\Sigma^0}$	$P_{\Sigma^0}$	$P_{\Sigma^0}$
-0.94	-0.18 $\pm$ 0.15	-0.34 $\pm$ 0.12	-0.09 $\pm$ 0.14	0.03 $\pm$ 0.11
-0.81	-0.22 $\pm$ 0.12	-0.07 $\pm$ 0.11	0.08 $\pm$ 0.11	0.21 $\pm$ 0.10
-0.69	-0.20 $\pm$ 0.13	-0.07 $\pm$ 0.12	-0.26 $\pm$ 0.13	-0.03 $\pm$ 0.11
-0.56	0.13 $\pm$ 0.15	-0.28 $\pm$ 0.15	-0.11 $\pm$ 0.14	-0.01 $\pm$ 0.14
-0.44	0.05 $\pm$ 0.18	-0.35 $\pm$ 0.16	0.16 $\pm$ 0.15	-0.11 $\pm$ 0.16
-0.31	-0.42 $\pm$ 0.18	-0.11 $\pm$ 0.18	-0.35 $\pm$ 0.19	0.10 $\pm$ 0.17
-0.19	-0.29 $\pm$ 0.19	-0.53 $\pm$ 0.18	-0.31 $\pm$ 0.20	-0.39 $\pm$ 0.17
-0.06	-0.20 $\pm$ 0.20	-0.40 $\pm$ 0.20	-0.03 $\pm$ 0.19	0.18 $\pm$ 0.17
0.06	-0.38 $\pm$ 0.20	-0.79 $\pm$ 0.19	-0.26 $\pm$ 0.19	-0.03 $\pm$ 0.14
0.19	-0.58 $\pm$ 0.19	-0.41 $\pm$ 0.21	-0.26 $\pm$ 0.18	0.06 $\pm$ 0.13
0.31	-0.50 $\pm$ 0.19	-0.16 $\pm$ 0.18	-0.20 $\pm$ 0.16	0.20 $\pm$ 0.12
0.44	-0.11 $\pm$ 0.19	-0.63 $\pm$ 0.18	-0.09 $\pm$ 0.17	-0.03 $\pm$ 0.12
0.56	-0.71 $\pm$ 0.21	-0.18 $\pm$ 0.19	-0.40 $\pm$ 0.18	0.29 $\pm$ 0.12
0.69	-0.06 $\pm$ 0.25	-0.25 $\pm$ 0.22	-0.08 $\pm$ 0.19	0.14 $\pm$ 0.13
0.81	-0.28 $\pm$ 0.36	-0.42 $\pm$ 0.34	-0.34 $\pm$ 0.32	0.24 $\pm$ 0.24
0.94	—	—	—	—

TABLE XXI: Associated Legendre function coefficients for the  $K^-p \rightarrow \pi^0\Sigma^0$  reaction for the four lowest beam momenta.

$p_{K^-} \pm \delta_p$ [MeV/c]	514 $\pm$ 10	560 $\pm$ 11	581 $\pm$ 12	629 $\pm$ 11
$B_1$	0.0895 $\pm$ 0.014	0.098 $\pm$ 0.011	0.0671 $\pm$ 0.0086	0.0425 $\pm$ 0.0073
$B_2$	0.007 $\pm$ 0.013	0.009 $\pm$ 0.010	0.0017 $\pm$ 0.0080	0.0016 $\pm$ 0.0070
$B_3$	-0.004 $\pm$ 0.012	0.0191 $\pm$ 0.0097	0.0012 $\pm$ 0.0077	-0.0011 $\pm$ 0.0066
$B_4$	0.0116 $\pm$ 0.0099	0.0031 $\pm$ 0.0078	-0.0117 $\pm$ 0.0062	-0.0037 $\pm$ 0.0052
$B_5$	-0.0050 $\pm$ 0.0095	0.0147 $\pm$ 0.0071	-0.0034 $\pm$ 0.0058	-0.0091 $\pm$ 0.0049
$\chi^2/\text{ndf}$	1.64	0.78	0.75	0.93

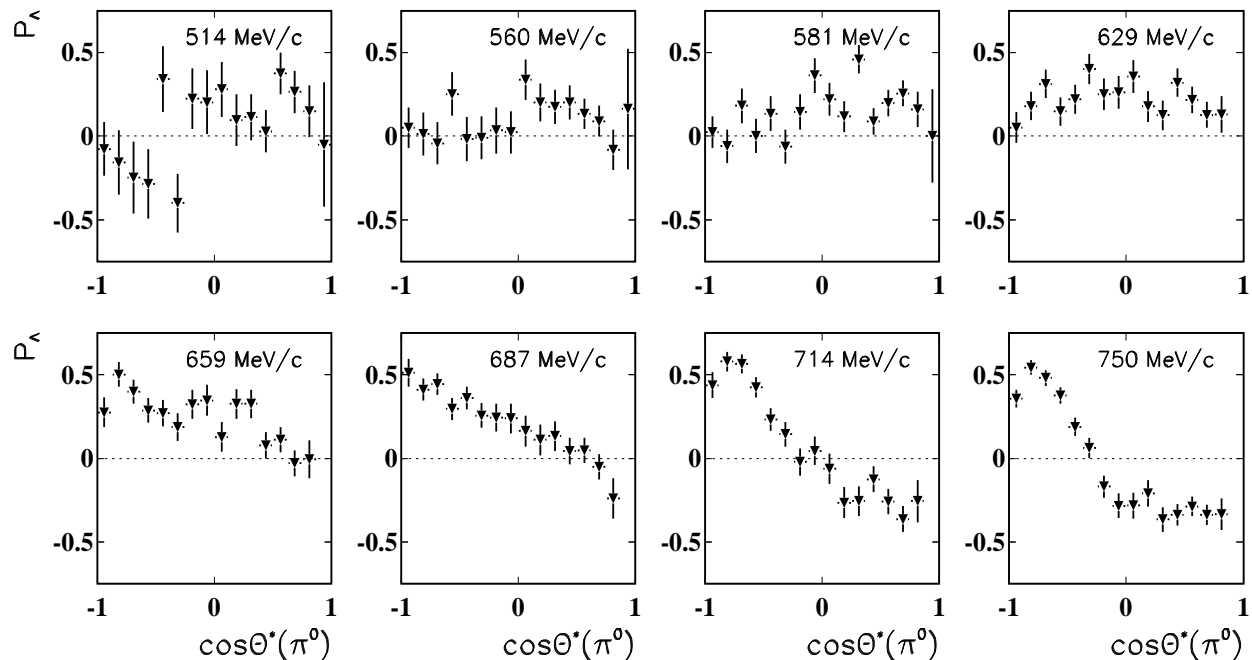


FIG. 11: Our results for the  $\Lambda$  polarization as a function of  $\cos\theta^*(\pi^0)$  for the  $K^-p \rightarrow \pi^0\Lambda$  reaction at the eight beam momenta.

TABLE XXII: Associated Legendre function coefficients for the  $K^-p \rightarrow \pi^0\Sigma^0$  reaction for the four highest beam momenta.

$p_{K^-} \pm \delta_p$ [MeV/c]	$659 \pm 12$	$687 \pm 11$	$714 \pm 11$	$750 \pm 13$
$B_1$	$0.0358 \pm 0.0070$	$0.0440 \pm 0.0067$	$0.0214 \pm 0.0067$	$-0.0137 \pm 0.0055$
$B_2$	$0.0024 \pm 0.0069$	$-0.0007 \pm 0.0068$	$0.0057 \pm 0.0071$	$-0.0096 \pm 0.0060$
$B_3$	$0.0079 \pm 0.0067$	$0.0087 \pm 0.0066$	$0.0057 \pm 0.0071$	$-0.0121 \pm 0.0062$
$B_4$	$-0.0073 \pm 0.0052$	$-0.0026 \pm 0.0050$	$0.0007 \pm 0.0050$	$0.0004 \pm 0.0043$
$B_5$	$0.0059 \pm 0.0049$	$0.0059 \pm 0.0047$	$0.0008 \pm 0.0047$	$-0.0028 \pm 0.0037$
$\chi^2/\text{ndf}$	1.24	1.52	1.15	1.20

## V. CONCLUSIONS

Differential cross sections and hyperon polarizations have been measured for  $\bar{K}^0n$ ,  $\pi^0\Lambda$ , and  $\pi^0\Sigma^0$  production in  $K^-p$  interactions at eight  $K^-$  momenta between 514 and 750 MeV/c. The experiment detected the multiphoton final states with the Crystal Ball spectrometer using a  $K^-$  beam from the Alternating Gradient Synchrotron of BNL. The results provide significantly greater precision than the existing data, allowing a detailed reexamination of the excited hyperon states in our energy range.

## Acknowledgments

This work was supported in part by DOE and NSF of the U.S., NSERC of Canada, the Russian Ministry of Industry, Science and Technologies, and the Russian Foundation for Basic Research. We thank SLAC for the loan of the Crystal Ball. The assistance of BNL and AGS with the setup is much appreciated.

- [1] C. Amsler *et al.* (Particle Data Group), Phys. Lett. B **667**, 1 (2008).  
 [2] R. Armenteros *et al.*, Nucl. Phys. B **21**, 15 (1970).  
 [3] M. Alston-Garnjost *et al.*, Phys. Rev. Lett. **38**, 1003 (1977).  
 [4] M. Alston-Garnjost *et al.*, Phys. Rev. D **17**, 2226 (1978).

- [5] G. W. London *et al.*, Nucl. Phys. B **85**, 289 (1975).  
 [6] A. Starostin *et al.* (Crystal Ball Collaboration), Phys. Rev. C **64**, 055205 (2001).  
 [7] S. Prakhov *et al.* (Crystal Ball Collaboration), Phys. Rev. C **69**, 042202 (2004).  
 [8] S. Prakhov *et al.* (Crystal Ball Collaboration), Phys. Rev.

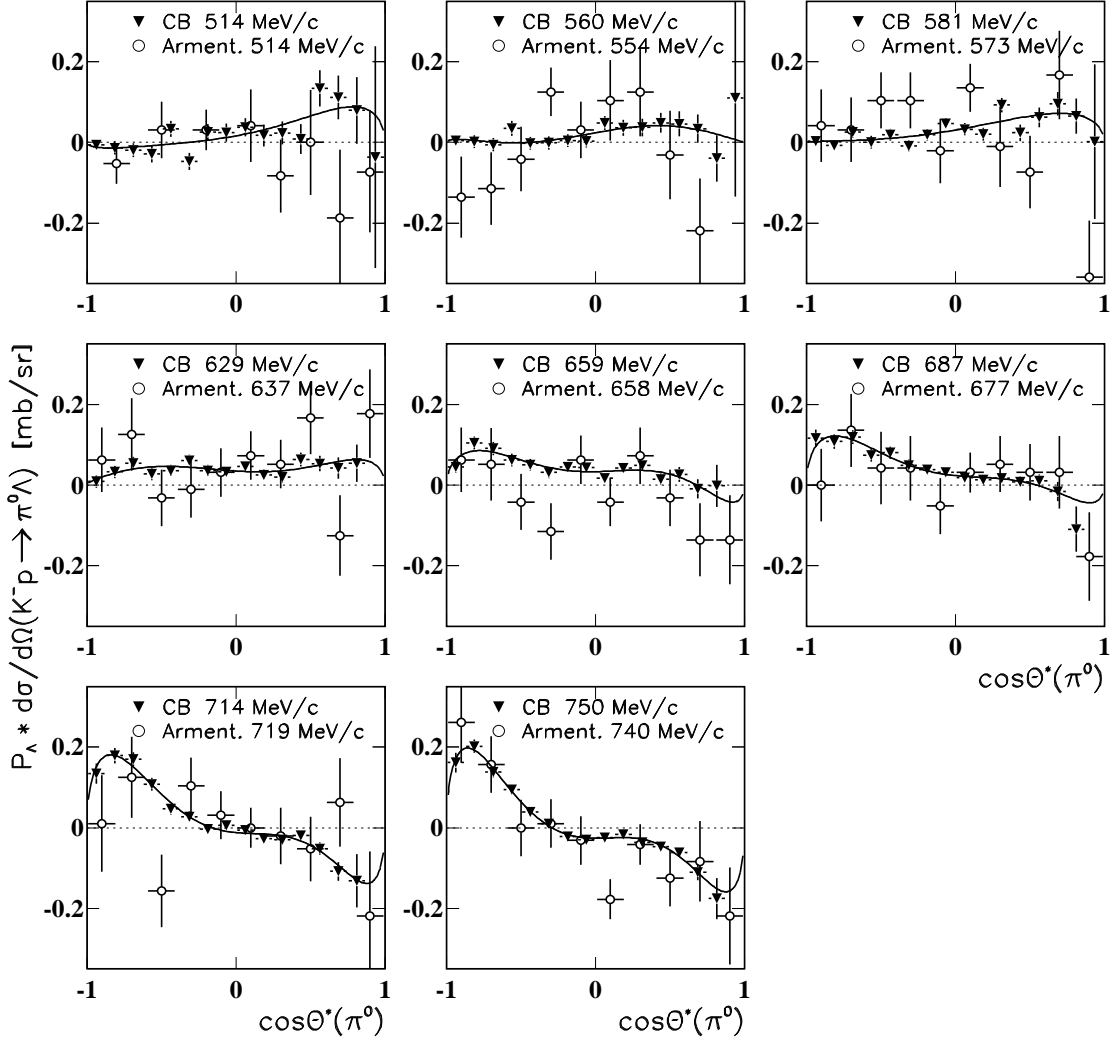


FIG. 12: Our results for the product of the  $\Lambda$  polarization and the differential cross section of  $K^- p \rightarrow \pi^0 \Lambda$  compared to the data from Armenteros [2]. The curves are the fits of our data to the first associated Legendre functions.

- C **70**, 034605 (2004).  
 [9] J. Olmsted *et al.* (Crystal Ball Collaboration), Phys. Lett. B **588**, 29 (2004).  
 [10] R. Manweiler *et al.*, Phys. Rev. C **77**, 015205 (2008).  
 [11] J. Olmsted, Ph.D. Dissertation, Kent State University (2001); <http://bmkn8.physics.ucla.edu/Crystalball/Docs/Theses/thesis-olmsted>.  
 [12] M. Borgh *et al.* (Crystal Ball Collaboration), Phys. Rev. C **68**, 015206 (2003).  
 [13] D. M. Manley *et al.* (Crystal Ball Collaboration), Phys. Rev. Lett. **88**, 012002 (2002).  
 [14] N. Phaisangittsakul, Ph.D. Dissertation, UCLA (2001); <http://bmkn8.physics.ucla.edu/Crystalball/Docs/Theses/thesis-nakorn>.  
 [15] J. A. Anderson, F. S. Crawford and J. C. Doyle, Phys. Rev. **152**, 1139 (1966).

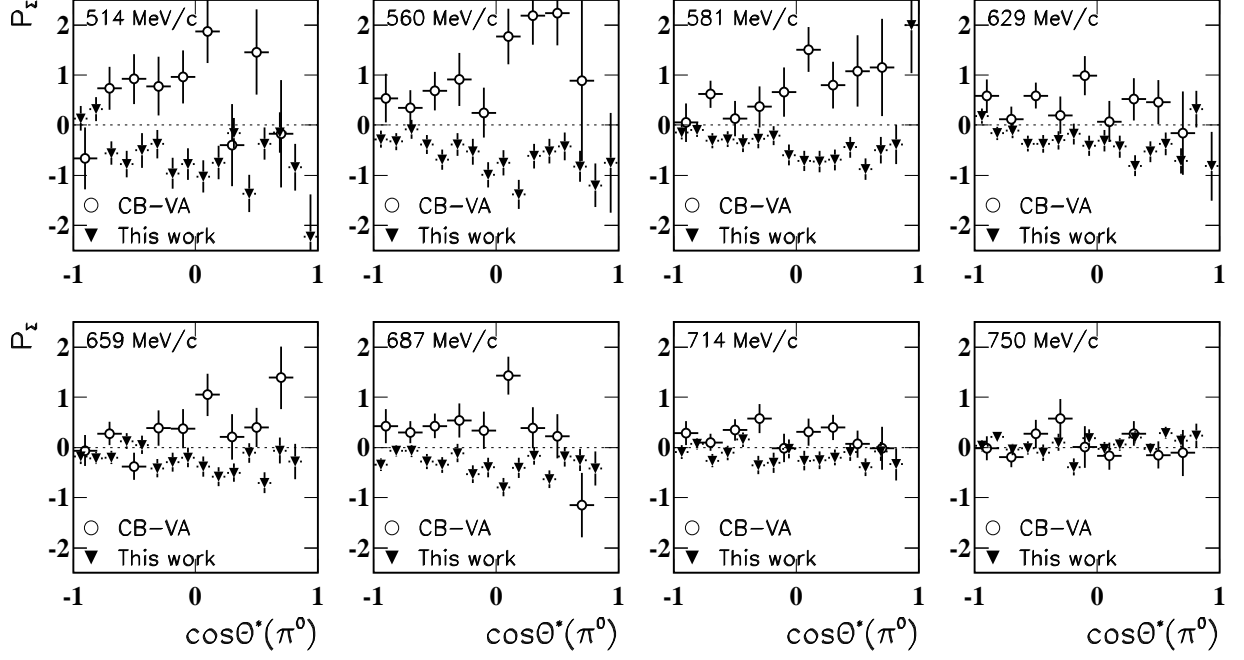


FIG. 13: Our results for the  $\Sigma^0$  polarization as a function of  $\cos\theta^*(\pi^0)$  for the  $K^-p \rightarrow \pi^0\Sigma^0$  reaction at the eight beam momenta, compared to the VA analysis [10]

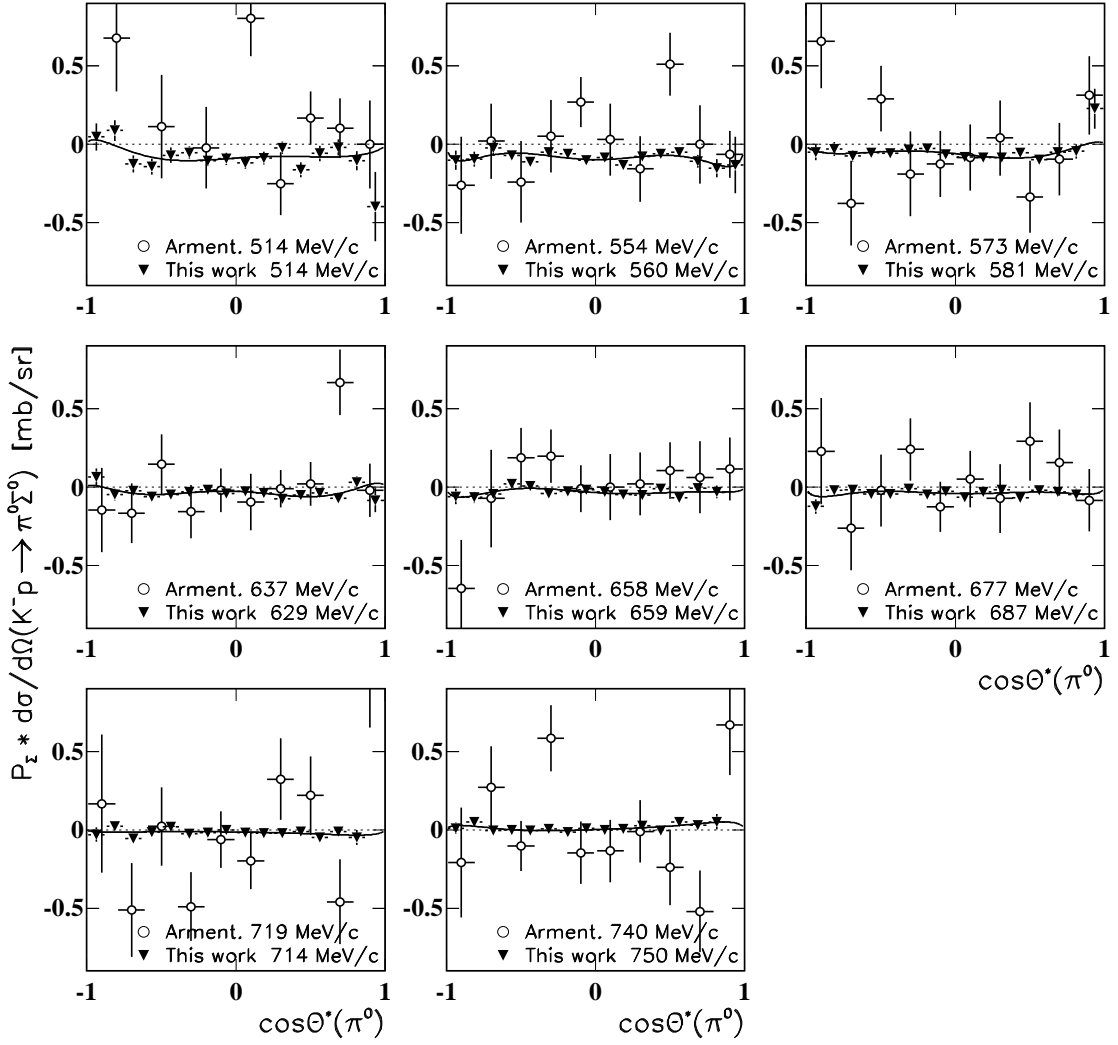


FIG. 14: Our results for the product of the  $\Sigma^0$  polarization and the differential cross section of  $K^- p \rightarrow \pi^0 \Sigma^0$  compared to the data from Armenteros [2]. The curves are the fits of our data to the first associated Legendre functions.